Title

Synthetic CT in Musculoskeletal Disorders

Journal

Investigative Radiology, 58(1)

ISSN

0020-9996

Authors

Lombardi, Alecio F

Ma, Ya-Jun

Jang, Hyungseok

et al.

Publication Date

2023

DOI

10.1097/rli.0000000000000916

Peer reviewed

HHS Public Access

Author manuscript

Invest Radiol. Author manuscript; available in PMC 2024 January 01.

Published in final edited form as:

Invest Radiol. 2023 January 01; 58(1): 43–59. doi:10.1097/RLI.0000000000000916.

Synthetic CT in Musculoskeletal Disorders: A Systematic Review

Alecio F. Lombardi, MD,

Ya-Jun Ma, PhD,

Hyungseok Jang, PhD,

Saeed Jerban, PhD,

Jiang Du, PhD,

Eric Y. Chang, MD,

Christine B. Chung, MD

Department of Radiology, University of California San Diego and the Research Service, Veterans Affairs San Diego Healthcare System, CA, United States.

Abstract

Repeated computed tomography (CT) examinations increase patients' ionizing radiation exposure and health costs making an alternative method desirable. Cortical and trabecular bone, however, have short T2 relaxation times, causing low signal intensity on conventional MR sequences. Different techniques are available to create a "CT-like" contrast of bone, such as ultra-short echo time (UTE), zero echo time (ZTE), gradient-echo (GRE), and susceptibility-weighted image (SWI) MR sequences, and artificial intelligence. This systematic review summarizes the essential technical background and developments of UTE, ZTE, GRE, SWI MRI sequences, and artificial intelligence, presents studies on research and clinical applications of "CT-like" MRI, and describes their main advantages and limitations. We also discuss future opportunities in research, which patients would benefit the most, the most appropriate situations for using the technique, and the potential to replace CT in the clinical workflow.

Keywords

Synthetic CT; CT-like MRI; Bone contrast MRI; UTE MRI; ZTE MRI; GRE; SWI; musculoskeletal disorders; CT ionizing radiation; ultrashort echo-time imaging; zero echo-time imaging

INTRODUCTION

Recently there has been an increased interest in magnetic resonance imaging (MRI) with "CT-like" contrast. The total number of CT examinations in the United States increased from 3 million in 1980 to 60 million in 2005[1]. In children, approximately 5 to 9 million CT examinations are performed annually[2]. Radiation exposure is a concern, especially in children, because they are more sensitive to radiation and begin accrual of life-long exposure

Correspondence to: Alecio F. Lombardi, MD, Department of Radiology, University of California San Diego, 9452 Medical Center Drive, La Jolla, 92037, CA, United States. alecio.lombardi@icloud.com.

doses that can ultimately lead to radiation damage[2]. Although the risk of radiation-induced cancer is much smaller than the natural risk of cancer, ALARA (As Low As Reasonably Acceptable) principles dictate that any radiation exposure carries some degree of risk and should be avoided if possible[3].

Implementing an additional "CT-like" contrast sequence to the conventional MRI protocol could also allow for a more efficient workflow by integrating this imaging information with conventional MR sequences without needing to schedule and perform a second imaging exam. It can also facilitate imaging registration and raise the diagnostic accuracy of certain bone diseases. In radiation oncology, it can improve PET/MRI coregistration and the precision of radiation therapies[4].

Imaging cortical and trabecular bone is challenging because of its short T2 (less than 0.5 ms)[5]. Standard MR sequences with routine slice thickness generally detect signals from tissues with T2 values of 10 ms or greater. Thus, when image sampling starts, the signal from cortical and trabecular bone has already decayed to its minimum and appears dark or anechoic. Cortical bone has a high proton density, with approximately 70% of its structure made of minerals and an organic collagenous matrix. The immobile macromolecules, strong dipole interactions and susceptibility, and surface relaxation contribute to the short T2 values. Densely calcified tissues such as cortical bone have low water content and present an low molecular "tumbling" rate which leads to rapid T2 relaxation without T1 relaxation, contributing to the absence of a signal on conventional MR sequences. Typically reported T1 values of cortical bone (between 140 to 540 ms) represent water either loosely or tightly bound to organic matrix protons[6,7].

Several techniques have been used to generate "CT-like" MRI contrast, such as ultra-short echo time (UTE), zero echo time (ZTE), and gradient echo (GRE) sequences (Figure 1). UTE MRI uses a very short echo time (TE) to acquire signals from short T2 tissues[8]. ZTE MRI begins imaging sampling in the presence of readout gradients, thus at zero echo time, also allowing the detection of signals from short T2 tissues[9]. One of the advantages of ZTE MRI is its low acoustic noise owing to the incremental evolution of gradients[10]. GRE uses a fast acquisition with a relatively short TE to detect signals from long T2 tissues. While conventional GRE sequences can reach TEs of about 10ms, some GRE sequences can achieve TEs of up to 1–2 ms. As a reference, tendons have mean T2 values within the range of 0.25 to 1.2 ms, cortical bone within 0.13 to 0.5ms, knee menisci about 4–8 ms, and ligaments around 4–10ms making it challenging to acquire high signals from these tissues[8]. On the other hand, UTE sequences can easily achieve TEs within the range of 0.032ms to 0.5ms on in vivo scans, with some studies reporting TEs of 8–10μs[11,12]. ZTE sequences have a TE of zero as imaging acquisition begins in the presence of the readout gradient, although coil switching from transmitting to receive modes results in a small dead-time of a few microseconds[13].

Deep learning has also been used to create synthetic CT from MRI using different MR sequences for input, including T1-weighted sequences[14] and multi-contrast DIXON type images[15]. "CT-like" contrast is then created using a bias-correction algorithm applied to the raw images[16]. Most of the recent advances in UTE and ZTE MR sequences were made

possible because of the high standards achieved by 3T MR systems that allowed faster scans, higher signal-to-noise ratio and better-quality images, and the ability to implement quantitative sequences. Moreover, UTE and ZTE sequences take advantage of the high-performance gradients systems, multi-channel coils, and rapid transmission radiofrequency technology[17].

This systematic review summarizes the essential technical background and developments of UTE, ZTE, GRE, SWI MRI sequences, and artificial intelligence, presents studies on research and clinical applications of "CT-like" MRI, and describes their main advantages and limitations. We also discuss future opportunities in research, which patients would benefit the most, the most appropriate situations for using the technique, and the potential to replace CT in the clinical workflow.

METHODS

This systematic review is in accordance with the Preferred Reporting Items for Systematic Reviews and Meta-Analyses (PRISMA) recommendations[18].

Eligibility Criteria

We considered ex vivo and in vivo studies using animal tissues, human tissues, and human subjects employing at least one method to generate synthetic CT images of cortical bone. The methods should include UTE, ZTE, GRE, Susceptibility Weighted Imaging (SWI) MR sequences, or artificial intelligence such as deep learning. We only included original research articles written in English and excluded reviews, conference abstracts, opinion articles, and letters to the editors.

Information Sources and Search

We used MEDLINE, EMBASE, and Scopus databases up until May 2022. The search strategy included terms in the title and abstract that referred to the inclusion criteria, such as "synthetic AND CT," "synthetic AND computed AND tomography," "synthetic AND MRI," "magnetic resonance imaging AND CT-like," "CT-like contrast AND UTE," "synthetic CT AND deep learning". A complete list of the terms used in the search strategy can be found in the Supplemental Material.

Data Collection Process and Data Items

One investigator performed data collection in a tabulated form. Extracted data items from studies included the number, age, and sex of participants, the main results, field strength, the main MRI sequence to create synthetic CT, scanner vendor, and the parameters used in the MRI protocol.

Risk of Bias in Individual Studies

The risk of bias in individual studies was assessed by one investigator using a modified version of the Quality Appraisal tool for studies of diagnostic Reliability (QAREL) adapted for this review[19]. Six specific items were used in the checklist and are listed in the Supplemental Materials.

Data Analysis

We reviewed the number, age, and sex of participants, the main study results, field strength, the main MRI sequence to create synthetic CT, the scanner vendor, and the parameters used in the MRI protocol. Critical technical development studies were included to give a background of each technique employed to generate a “CT-like” contrast MRI. A meta-analysis was not suitable considering the heterogeneity in the evaluated data items, different diseases, anatomical regions, clinical outcomes, the distinct methods for generating synthetic CT images, and statistical analysis. Therefore, a narrative review was performed, highlighting relevant research and clinical applications of the five main methods to create synthetic CT images (UTE, ZTE, GRE, SWI, Deep Learning).

RESULTS

Study Selection

The database and reference list of studies returned 719 articles. The final review included 75 full-text articles. A flowchart of the search results, screening, exclusions, and the final number of studies included in the review is presented in Figure 2.

Study Characteristics

The characteristics of studies in the final review are in Table 1. Nine studies used UTE MRI to quantify the signal-to-noise and contrast-to-noise ratio of bone. Eighteen studies used UTE MRI for T1, T2*, bound water, pore water, porosity index, macromolecular fraction, or macromolecular density quantification. Eight studies used UTE MRI in practical clinical case scenarios to evaluate intermodality agreement with CT. Fourteen studies used ZTE MRI in practical clinical case scenarios to assess intermodality agreement with CT or echo-planar imaging (one study of diffusion in cortical bone). Nine studies included GRE MRI in clinical case scenarios to assess intermodality agreement with CT or arthroscopy. Ten studies included SWI MRI in clinical case scenarios to assess intermodality agreement with CT or radiographs. Finally, six studies used deep learning to create synthetic CT images and assess intermodality agreement with CT. Secondary outcomes included inter-rater and intra-rater agreement, comparisons between synthetic CT and conventional MRI, quantitative properties obtained from synthetic CT and biomechanical properties of bone, and accuracy for specific diagnostics.

The systematic review analysis included data from 1,662 human subjects, 229 human tissues, and 17 animal tissues. The mean age ± standard deviation of the human participants was 47.8 ± 17.6. Forty percent were female.

Forty-eight percent of the studies used scanners from GE (GE Healthcare Technologies, Milwaukee, WI, USA), 37.3% from Siemens (Siemens Medical Solutions, Erlangen, Germany), and 10.7% from Philips (Philips Healthcare, Best, The Netherlands). Seventy-seven percent of the studies chose 3T as the field strength, 14.8% chose 1.5T, while the remaining 8.2% included at least two field strengths (1.5T, 3T, or 7T) or only 7T. Scan times for one in vivo independent synthetic CT acquisition varied from 2 min to 15 min. Signal-to-noise ratios of cortical bone varied from 10 to 70, whereas the contrast-to-noise

ratio between cortical bone and the surrounding short T2 tissues ranged from 12 to 30. The signal-to-noise ratio of cortical bone increased 1.7 times on 7T field strength compared to 3T, whereas T2* values decreased by half on 7T vs. 3T, according to one study. Typical T1 measurements of cortical bone varied from around 140ms (bound water) to 306ms (pore water), whereas T2* ranged from around 0.29ms (bound water) to 4.33ms (pore water). Moreover, moderate to strong correlations were found between bound water, pore water, and bone porosity index estimated through UTE MRI and cortical bone mechanical properties, μCT porosity, μCT bone density, and age. When assessing the similarity between synthetic CT and CT images, all methods (UTE, ZTE, GRE, SWI, and deep learning) showed high intermodality agreement and excellent inter-rater agreement.

Risk of Bias in Individual Studies

The results of the risk of bias in individual studies are in Figure 3. Overall, the quality of the evidence was high for studies investigating intermodality agreement between synthetic CT and CT and moderate for studies investigating quantitative measurements of bone. The questions in which studies performed the lowest were if the investigators were blinded to themselves or other data analysts and if appropriate statistics were performed. One should consider, however, that many studies of quantitative imaging of cortical bone are still in the pre-clinical and translational stages and, thus, are mainly based on animal or human tissues, with fewer observations.

UTE MRI

Technical Background

UTE MRI uses short radiofrequency pulses due to the rapid transverse relaxation of short T2 tissues. After a brief time, image data acquisition begins simultaneously with gradient ramp-up. In 2D UTE MRI, the radiofrequency pulse is truncated, and the acquisition is divided into two stages, each preceded by a radiofrequency pulse and a slice selective gradient, followed by readout gradients. Both stages are added to generate one radial spoke of k-space. The process is then repeated at 360° to radially fill k-space, which is later reconstructed into cartesian coordinates (Figure 4). In 3D UTE MRI, either a rectangular non-selective or a soft selective radiofrequency pulse can be used, and the gradients can be applied in all three directions generating a “koosh ball” or a conical k-space sampling pattern[20] (Figure 5).

On UTE MRI, signals from long T2 tissues reduce the image contrast. Also, due to the non-cartesian k-space sampling, chemical shift artifacts can occur in transitions between water and fat[21]. Several methods can increase the contrast between short and long T2 components. A long 90° pulse followed by a crusher gradient will suppress signals from long T2 tissues, with signals from short T2 tissues minimally affected due to significant decay during the long pulse duration[22]. However, this technique suffers from off-resonance effects. Another technique uses two images with different TEs followed by subtraction later echoes from the first to create a short T2 contrast[23]. Disadvantages of this technique include reduced signal-to-noise ratio, susceptibility artifacts, and a residual signal from muscle and fat. One alternative is to scale down the free induction decay to reduce signals from muscle and

fat, also called “UTE with rescaling echo subtraction”[24]. Inversion recovery techniques, on the other hand, use adiabatic pulses, which are insensitive to B_1 inhomogeneities, centered in the water resonance frequency to invert the magnetization from long T2 components (single inversion recovery)[25]. This technique can be combined with a fat-suppression pulse or a second inversion recovery pulse centered in the fat resonance frequency to increase further the contrast of short T2 components (dual inversion recovery)[26,27]. Although a fat-suppression pulse can increase contrast, it may reduce signals from short T2 tissues[28]. A single-point Dixon method has been described for fat suppression on UTE imaging, allowing more accurate fat and water separation[29].

UTE MRI requires a short coil “ring down” time to switch from receiving to transmit modes to prevent signal loss from short T2 tissues. Also, the image quality depends on a short ramp-up time and maximum strength of gradients.

Morphological Bone Imaging with UTE MRI

Cortical bone presents different transverse relaxation components reflecting distinct proton origins[30], including collagen matrix (~12μs), collagen side-chains (~60μs), water firmly attached to collagen (~100–250μs), and water loosely attached to collagen or free within bone pores (~400–500μs)[31]. Therefore, acquiring signals from cortical or trabecular bone is challenging. However, significant progress has been made on UTE MRI sequences and there is enough evidence showing the ability of UTE in providing high-resolution, high signal-to-noise, and high contrast-to-noise ratio clinical images of cortical and trabecular bone[11,24,32,33]. Several studies have also investigated the ability of UTE sequences to serve as a surrogate of CT images applied to everyday clinical case scenarios.

Ma et al. compared CT and 3D IR-UTE Cones MRI on 11 shoulder specimens before and after inducing a glenoid bone fracture and three patients with shoulder pain and glenohumeral instability[34]. Glenoid diameter and glenoid bone loss measurements on both methods were compared across two readers and showed high inter-rater and intermodality agreement, confirming that UTE MRI could be used as a surrogate for CT (Figure 6).

Finkenstaedt et al. investigated the diagnostic performance of conventional and UTE MRI in the lumbar spine of 46 cadaveric specimens with pars interarticularis fractures[35] and concluded that UTE MRI had higher accuracy.

Afsahi et al. recently showed the feasibility of a 3D UTE Cones MRI with a slab-selective radiofrequency pulse to image the spine in healthy volunteers and patients with back pain showing excellent intermodality agreement with CT[36] (Figure 7). The thoracic and lumbar spines suffer from higher artifacts from respiratory movements, which causes blurring of the anterior contours of the vertebral bodies. However, a slab-selective radiofrequency pulse can partially reduce image blurring in the vertebral bodies (Figures 7 and 8).

Deininger-Czermak et al., on the other hand, compared UTE, an optimized 3D-multi-echo in-phase gradient-echo sequence (FRACTURE), and CT in the assessment of craniocervical junction (CCJ) degeneration[37]. Degenerative changes in the CCJ showed a good interrater

and intermodality agreement between MRI sequences and CT, without differences between UTE and FRACTURE.

UTE MRI has also been used to detect fractures of the tibial eminence in children, demonstrating equivalent sensitivity and specificity to CT[38]. For fracture detection, UTE improved agreement between readers on the size, number, displacement, and grade of fracture fragments, leading to a change in consensus in 20% of the cases.

UTE MRI has also been used to study the temporomandibular joint morphology and evaluate medication-induced osteonecrosis of the jaw, with high anatomical correlation with CT images[39,40].

Quantitative Bone Imaging with UTE MRI

T1 and T2* relaxation measurements—One of the main advantages of UTE MRI is the possibility to quantify relaxation times and the concentration of total, bound, and free water in the cortical bone.

T1 relaxation times can be measured by applying a 90° pulse followed by a crusher gradient to suppress signals from long T2* components and multiple consecutive UTE acquisitions with progressively increasing saturation recovery times[41]. Saturation-recovery is effective but time-consuming. Inversion recovery-based UTE methods, on the other hand, are inadequate for T1 estimation of short T2* tissues because their magnetization cannot be fully inverted by the long duration inversion pulse but only saturated due to its very fast transverse relaxation. Other options are using variable repetition times (TR)[42] or variable flip angles (VFA)[43], which require a rigorous correction for B1 inhomogeneities. T2* relaxation times are measured using multiple acquisitions with increasing TEs and fitting the data into exponential equations.

Reichert et al. studied cortical bone imaging using a 2D UTE MRI with inversion recovery pulses and later echo images to generate contrast between short and long T2 tissues in seven healthy volunteers and ten patients[44]. Mean T1 relaxation times among the volunteers ranged from 140 to 260 ms, whereas mean T2* ranged from 420 to 500 μs.

Du et al. described a 2D UTE MR sequence with TE of 8 μs to image cortical bone at 3T applied to five healthy volunteers[41]. The sequence involved an adiabatic inversion recovery pulse in suppressing the magnetization of long T2 components. They also used an external phantom to calculate the water concentration, multiple echoes to estimate the T2*s of short T2 tissues, and saturation recovery to estimate the T1 relaxation times. The sequence showed cortical bone with high resolution, signal-to-noise, and contrast-to-noise ratio. The mean T1 was 223 ± 11 ms, and the mean T2* was 390 ± 19 μs in the healthy volunteers. Water concentration was 21.7 ± 1.3% assessed with IR-UTE (Figure 10).

Nazaran et al. investigated the performance of a 3D UTE sequence with cones k-space trajectory and TE of 32 μs, associated with an adiabatic inversion recovery pulse (3D IR-UTE) in the hip of four healthy volunteers[45]. T2* of cortical bone was estimated using

multiple echoes and mono-exponential fitting. High cortical bone contrast was achieved, and the T2* ranged from 330 to 450 μs.

Bound and Pore water estimation—In cortical bone, water can be loosely or tightly bound to the organic matrix and minerals. Bound water (BW) has very short T2 or T2* relaxation times, whereas free water exists in the pores of cortical bone; thus, the name pore water (PW), which has short T2* relaxation times that are significantly longer than BW. The previously described methods can quantify T1 and T2* for cortical bone but cannot differentiate between relaxometry of BW and PW. By measuring these different relaxation times, one may estimate the composition of the different bone compartments, for example, the water concentration, organic matrix (collagen), mineralization, or porosity. Quantitative maps can then be created[46].

Several strategies are used to estimate cortical bone water, including the direct signal measurement of short T2 tissues by UTE MRI using a water phantom as a reference[47,48], signal measurement using multiple TEs and multi-component T2* model fitting with micro-CT as a reference[49,50], calculating the bone porosity index by the rate of signals between two echoes[51], estimating the macromolecular fraction (MMF) of bone by magnetization transfer (MT) model fitting[52,53], using an inversion recovery pulse to null the signals from long T2 components[54,55], among others[56]. Moreover, there is strong evidence that bone water estimated through UTE MRI is correlated with age and microstructural properties of cortical bone.

The total bone water and the pore water fraction in cortical bone estimated by UTE MRI are positively correlated with age[57] and negatively correlated with bone mineral density[58] measured by CT. Another recent study showed that the cortical porosity index measured by UTE MRI correlated negatively with bone stiffness[59]. Jerban et al. conducted several studies using UTE-MT modeling and T2* tricomponent analysis to estimate cortical bone bound and pore water, bone porosity index, proton density fractions, and macromolecular fractions in cortical bone using μCT as a reference. The investigators showed consistently that higher pore water concentration, higher porosity index, lower proton density, and macromolecular fractions are correlated with bone mineral density and CT porosity[50,60–65].

Technical Limitations of UTE MRI

UTE MRI has limitations. For example, the signal from short T2 tissues has a broad spectrum (amplitude versus frequency) which makes them prone to off-resonance effects, primarily on 2D multislice acquisitions or using fat-suppression techniques[8]. UTE MRI is subjected to eddy current artifacts due to fast switching and strong gradients. The additional magnetization preparations required for suppressing long T2 tissues and the two excitations by k-space sampling necessary on 2D UTE increase the scan time, although using multiple spokes can overcome this limitation[66]. The radial center-out k-space sampling is subject to chemical shift artifacts due to the typical ring-shaped point spread function[21].

ZTE MRI

Technical Background

The basic principle of ZTE MRI is to apply a radiofrequency pulse after the readout gradients have ramped up, thus with effective echo time near 0, using non-cartesian projection reconstruction k-space sampling[10]. As in UTE MRI, a bias correction algorithm is applied to the raw images, creating "CT-like contrast"[16,67]. First described as Back-projection Low Angle Shot (BLAST) to image solids or liquid-like solids, zero echo time imaging used gradient ramp-up, followed by radiofrequency excitation, then gradient ramp-down as in UTE and conventional MRI sequences[68]. Later, though, an optimization using small incremental gradients was proposed allowing ultra-fast image acquisition with low acoustic noise, called Ultra-fast Imaging Using Low Flip Angles and Fids (RUFIS)[69] (Figure 11B). Examples of the 3D ZTE sequence applied on the ankle, and the metatarsophalangeal joints can be seen in Figures 12 and 13.

ZTE MRI contrast is based mainly on the tissue's proton density (PD) and T1 relaxation time, but magnetization preparation modules can create distinct contrast mechanisms. For example, using multiple echoes and gradient refocusing, one can produce T2 and T2* contrast[70,71]. Also, variable flip angle (VFA) and inversion recovery techniques can be associated with ZTE MRI to generate T1 maps[72,73]. Diffusion imaging using ZTE has been described using a combination of eddy-current compensation methods and phase cycling[74].

As the k-space sampling starts with the gradients ramped up, the center of the k-space is always lost[75] (Figure 11B). The number of missed data points depends on machine-specific hardware factors such as the coil ring-down time and the filter bandwidth. In general, for a small number of missed data points, mathematical reconstructions using linear algebra can be used for their recovery[75]. If more data points are missed, one can acquire them separately using radial k-space sampling with weaker gradients, also called Water- and Fat-suppressed Proton Projection MRI (WASPI)[76]. Another method is to acquire the points at the center of the k-space using Cartesian sampling one point at a time with step-through gradient evolution, and the points at the periphery using non-cartesian radial sampling, known as Pointwise Encoding Time Reduction with Radial Acquisition (PETRA)[77]. A third method is to use multiple sets of radial acquisitions with decreasing gradient strengths so that in the center of the k-space, the data is acquired in a single pointwise fashion. In contrast, in the periphery, data acquisition forms multiple shells with different spokes densities, a method called Hybrid Filling of the dead-time gap for Faster zero echo time Imaging (HYFI)[78].

Another challenge in ZTE MRI is that because gradients are applied before the radiofrequency excitation, the bandwidth of the pulse must be high enough to span the whole sample uniformly; otherwise, the pulse will induce slice-selectivity, creating artifacts[79]. Also, in radial k-space encoding, there is no distinction between phase and frequency encoding gradients. If an increase in the spatial resolution is desired, the total number of projections must also be increased, thus increasing the scan time[80]. Aliasing artifacts are common in ZTE MRI because any tissue outside the region of interest will generate a signal at zero echo time. Attention to the coil material and size may overcome

these limitations[81]. Chemical shift artifacts are common but can be mitigated using larger pixel bandwidths, fat suppression, water/fat separation and selection of in-phase images[82].

Clinical and Research Applications of Synthetic CT using ZTE MRI

Several studies have shown the potential of ZTE MRI as synthetic CT in the clinical setting. For example, in a cohort of 34 patients, ZTE MRI showed high intermodality and inter-rater agreement with CT for glenoid morphology, injury or disease, and superior performance compared to conventional MRI[67]. Mello et al. showed high inter-rater and intermodality agreement between ZTE MRI and 3D CT in the measurement of glenoid bone defects in 10 patients with symptoms of glenohumeral instability[83]. Figures 14 and 15 show examples of ZTE MRI for the evaluation of fractures and identification of bone fragments in the shoulder. High intermodality and inter-rater agreement between ZTE MRI and CT were also found when evaluating cervical neuroforaminal stenosis[84] (Figure 16), lumbar degenerative changes[85], and sacroiliac joint structural lesions[86]. In addition, ZTE MRI can be used to evaluate ossification of the posterior longitudinal ligament of the spine[87,88](Figure 17).

Another study with 28 patients evaluated for femoroacetabular impingement or dysplasia showed excellent inter-rater and intermodality agreement in several morphological measures between ZTE MRI and CT[89]. ZTE showed high intermodality agreement with CT for the evaluation of heterotopic ossification around the hip[90] and degenerative changes in the knee[91].

Sandberg et al. investigated the performance of synthetic CT and synthetic radiographs through ZTE MRI in the extremities of pediatric patients with and without pathology[92]. The authors found that image quality was diagnostic and comparable to CT. Excellent results were also found using ZTE MRI in the temporomandibular joint[93].

ZTE MRI was also applied to diffusion-weighted imaging (DWI). Yuan et al. described a RUFIS sequence modified for diffusion preparation, including eddy current compensation and phase cycling to avoid T1 contamination[94]. The sequence was tested in the joints of 10 pediatric patients and compared to echo-planar imaging (EPI) DWI. Results showed distortionless images with accurate ADC measurements. Similar results were later confirmed in 39 pediatric patients referred for MRI of the extremities[95].

Comparisons between UTE and ZTE MRI

Larson et al. investigated differences between UTE and ZTE MRI at 7T using identical parameters and fat-suppression pulses to increase the image contrast of short T2 tissues in the knee and ankle of seven healthy volunteers[96]. ZTE had background signals from the coil components and suffered from blurring and a signal dropout at the edges of the field-of-view (FOV) but had the advantage of low acoustic noise. UTE MRI was more flexible because it allowed choosing between 2D and 3D acquisitions, 3D with and without slab-selectivity, more flexible FOV and flip angles (FAs), and variable TEs compared to ZTE. However, it was very sensitive to gradient fidelity. Artifacts due to off-resonance effects were present in both methods. The signal-to-noise efficiency in imaging the cortical bone was similar between UTE and ZTE.

Gradient Echo MRI

Technical Background

On GRE sequences, the radiofrequency pulse is applied before the spatial encoding gradients, which are used to generate an echo (signal). “CT-like” contrast images are created by subtracting all the pixels in the image by the lowest mean value of the tissues surrounding the bone structures, resulting in near-zero signal intensity in the soft tissues but a bright signal in the bone. Investigators have used the Fast Low Angle Shot (FLASH) and the Volumetric Interpolated Breath-hold Examination (VIBE) MR sequences to create synthetic CT[97]. Additional fat-saturation using spectral fat-suppression or the Dixon method can further improve contrast.

Recently a new 3D gradient echo sequence to generate CT-like contrast was described and implemented in a Philips scanner (Philips Healthcare), named Fast field echo Resembling a CT using restricted echo-spacing (FRACTURE)[98]. Its principle is based on acquiring multiple in-phase TEs equally spaced, followed by magnitude summation of images from all echoes and subtracting the last echo from the summated images to invert the grayscale. The authors advocate that the in-phase TEs minimize chemical shift and reduce additional dephasing caused by T2* decay helping to reduce signal loss at bone interfaces.

Another synthetic CT sequence based on gradient-echo MRI recently described is called 3D-Bone[99]. It is a 3D spoiled GRE with a short in-phase TE, small flip angles to maximize proton density (PD) contrast, and without fat suppression. The k-space sampling is acquired with a stack of stars, applying Cartesian encoding in the through-plane and radial encoding in the in-plane directions.

One disadvantage of gradient-echo sequences compared with UTE and ZTE MRI is that the predominant contrast is T2*, so field inhomogeneities caused by metals, foreign bodies, or iron deposits may cause strong susceptibility artifacts.

Clinical and Research Applications of Synthetic CT using GRE MRI

The glenoid and humeral head measurements have been studied using a Dixon 3D-dual-echo-time T1w FLASH MRI and 3D CT as a reference[100]. The water-only image was reconstructed in 3D. The investigators found no statistical difference between the imaging methods. The results were later confirmed comparing Dixon 3D-dual-echo-time T1w FLASH MRI with arthroscopy[101], with the mean absolute error between methods lower than 2.21%. Dixon T1w 3D FLASH MRI was also validated in the assessment of glenohumeral instability using a semiautomatic segmentation method and CT as a reference[102]. The differences in 88% of all measures were lower than 2% between the methods.

3D VIBE MRI with water excitation was studied in 12 shoulders of patients with glenohumeral instability[103]. The measured differences for humeral height, glenoid height, and glenoid width were borderline statistically significant but failed to be significant when considering multiple comparisons.

Dixon T1w 3D FLASH MRI was also studied in the hip in 17 patients with suspected femoroacetabular impingement for presence and location of cam deformity, anterior-inferior iliac spine variant, lateral center-edge angle, and neck-shaft angle using CT as a reference[104]. There was 100% agreement for the presence and location of cam deformity, 89.5% agreement for anterior-inferior iliac spine characterization, and 64.7% agreement for lateral center-edge angle and neck-shaft angle. 3D VIBE MRI also showed excellent intermodality agreement with CT to measure the acetabular's center edge angle, Tonnis' angle, anterior and posterior acetabular sector angle, and acetabular version in 550 patients[105].

Other studies comparing GRE-based synthetic CT with CT in musculoskeletal diseases include the evaluation of lumbar spine pars interarticularis fractures using 3D VIBE MRI[106] and bone destruction patterns and periosteal reaction using T1-FFE MRI sequence (Philips Healthcare)[107]. Both studies showed a near-perfect correlation between synthetic CT MRI and CT images.

Comparisons between UTE and GRE MRI

A recent comparison between dual-echo UTE MRI and 3D-multi-echo in-phase gradient-echo (FRACTURE) MRI using CT as a reference in assessing craniocervical junction qualitative and quantitative measurements showed high inter-rater and intermodality agreement for both MRI methods[108]. According to the authors, UTE would be recommended due to a better tradeoff between the contrast-to-noise and scan time.

3D T1-weighted spoiled GRE has also been used with a stack of stars k-space sampling on a Philips scanner (Philips Healthcare) followed by image inversion to generate CT contrast and compared to a 3D UTE MR sequence using CT as a reference[109]. Both methods achieved high sensitivity, specificity, and accuracy for fractures (0.95, 0.98, and 0.97 for 3D T1 Spoiled GRE (SGRE) versus 0.91, 0.96, and 0.95 for 3D UTE, respectively). Agreement between 3D T1 SGRE was slightly higher than 3D UTE for degenerative changes.

Figure 18 shows an example of a high-resolution image of the calcaneus using a 3D T1-weighted GRE sequence and image inversion to produce a bright signal for the cortical and trabecular bone.

Susceptibility Weighted Imaging (SWI)

Technical Background

Susceptibility weighted imaging (SWI) uses the principle of different changes in the image phase caused by blood, iron, and calcification across the tissues[110]. It is based on a GRE sequence with a small flip angle and increased TE, thus weighted towards T2*. The phase component of the raw data is then used to create a mask, which is multiplied by the magnitude image to highlight susceptibility effects (Figure 1D). Paramagnetic substances such as deoxyhemoglobin, ferritin, and hemosiderin shift the phase positively, whereas diamagnetic substances like calcium shift the phase negatively, creating contrast[111].

Clinical and Research Applications of Synthetic CT using SWI

Several studies showed the high performance of SWI MRI for evaluating musculoskeletal disorders compared with conventional MR sequences. Ulas et al. showed higher accuracy of SWI MRI for detecting bone erosion in the hands compared with T1-weighted images only101 and with T1-VIBE MRI using CT as a reference[112]. The same group also showed high accuracy of SWI in detecting foraminal stenosis in the cervical spine[113], in the differentiation between osteoblastic and osteolytic metastasis in the spine[114], differentiation between sclerotic and non-sclerotic Modic changes in the spine[115], in the detection of vertebral body fractures[116], detection of subacromial spurs[117], osteophytes and disc herniation[118], angle measurements in the hip[119], and erosions/sclerosis in the sacroiliac joints of patients with axial spondyloarthritis[120]. The studies included representative patients and controls for each diagnosis, had high inter-reader reliability, and the scan time was around 5 min. One clear advantage of SWI MRI over T1-weighted or T2- weighted images is its higher contrast between bone and soft tissues, which creates difficulties in evaluating neuroforaminal stenosis, femoroacetabular angles, or osteolytic lesions. Some challenges, however, include the higher susceptibility in 3T or 7T field strengths, which limits its use to 1.5T scanners, and phase shifts between bone and fat that may create artifacts within the bone's medullary cavity.

Artificial Intelligence (AI) to create Synthetic CT from MRI

Technical Background

Deep learning is based on computer algorithms that automatically extract features from images using multiple layers of neural networks, followed by minimization of loss functions to accomplish classification or regression tasks. There is high flexibility in the input images, including T1-weighted, T2-weighted, Dixon, UTE, or ZTE MRI sequences, or a combination of these[14]. The most studied deep learning architectures for translation of MRI into CT images are U-net and Generative Adversarial Networks (GANs)[121,122]. In U-net, an encoder automatically extracts features from images in a downsampling path, and a decoder organizes those features in an upsampling track creating a localization map that is translated into the synthetic image. In GANs, a generator creates synthetic images, and a discriminator compares them to actual data (Figure 1E). The goal is to generate synthetic images similar to authentic ones. GANs seem to create less noisy images than other deep learning architectures[123].

Challenges of deep learning-based methods include susceptibility to the input data, the high number of examples necessary to train the model, and the heterogeneity of model performances among different sites. For example, chemical shift artifacts can cause the model to underperform, creating blurred images when using out-of-phase or ZTE images as inputs[124,125].

Clinical and Research Applications of Synthetic CT using AI

Most research in deep learning-based methods of synthetic CT generation focuses on diagnosis and treatment planning in radiation oncology. CT is essential for radiotherapy dose calculation as it provides information on the electron density of tissues expressed

in Hounsfield Units. Also, CT fused with PET images is important in diagnosing and assessing response to treatment. However, the signals from synthetic CT images can be quantitatively scaled for radiodensity estimation in Hounsfield Units, making it interesting for replacing CT and allowing its use in radiation dose planning, MRI-only radiotherapy planning, or PET attenuation correction[126,127]. Fewer studies applied deep learning methods of synthetic CT generation specifically to musculoskeletal disorders. Nevertheless, some studies showed high agreement between synthetic images generated by deep learning and CT, including in the evaluation of morphologic parameters of the hip[128], surgical planning of the lumbar spine[129,130], creation of 3D printed models for surgical planning[131], detection of structural lesions in the sacroiliac joints[132], in the treatment planning of bone metastasis by MRI-guided high-intensity focused ultrasound (MRI-HIFU)[133].

Discussion

In this systematic review, we demonstrated that synthetic CT images or MRI with “CT-like” contrast could be generated using five main techniques: UTE, ZTE, GRE MRI sequences, SWI, and deep learning. Suggested MRI protocols for each technique can be found in table 2. Overall, 3T field strength was preferred over 1.5T across the three main MRI scanner vendors. Among GRE MRI sequences, T1FLASH and T1VIBE were dominant, whereas, for deep learning architectures, U-net and GANs were the most commonly used. Inter-rater and inter-modality agreement were high between the synthetic images created with the different techniques and CT. Most studies scored high in the QAREL checklist for reproducibility of MRI protocol. The studies that scored low were due to the lack of inter-rater and intra-rater analysis; however, these were mainly pre-clinical and translational investigations, using animal or human tissues with fewer observations, essential for technical advances and standardization of protocols that will later be used in clinical studies.

UTE MRI can quantify cortical bone T1, T2*, bound, and pore water, thus estimating bone porosity and water concentration. Quantitative and compositional MRI of bone can add precise and individualized information for patients with osteomalacia, osteoporosis, or athletes at risk for stress fractures. It can also be a supplementary tool over bone mineral density when monitoring response to treatment for osteoporosis. For example, there is evidence that changes in the microstructure and porosity of bone, not only the degree of mineralization, are associated with its tensile properties[134]. Also, in a large cohort study of men and women over 55, only 44% of fractures occurred in women with X-ray absorptiometry T-scores below −2.5 (definition of osteoporosis)[135]. Therefore, bone mineral density cannot solely predict or explain the fracture risk in patients with osteoporosis, and a new biomarker is desirable.

ZTE MRI is near-silent, which is essential in neonatal or pediatric patients who need to examine while asleep, in patients with hyperacusis or autism spectrum disorder, and in some older patients who are highly sensitive to the noise from MRI scanners[10]. Compared to UTE MRI, ZTE MRI synthetic CT images can depict bone with similar high contrast to the surrounding soft tissues, high inter-modality agreement with CT, similar levels of signal-to-noise ratio, and comparable scan time-efficiency.

Challenges of UTE MRI include the need for high-fidelity gradients to reduce off-resonance artifacts, whereas ZTE MRI may present blurring and signal dropping at the edges of the field-of-view[96]. Moreover, both sequences require advanced software package implementations. Since no reimbursement code exists yet for this emerging technology, it will initially come with increased costs for radiology providers that intend to implement it in their clinical practice.

Gradient echo-based sequences can also be used to create synthetic CT images. However, although already widely available throughout different vendors, it is still unclear how the inversion of images necessary to create “CT-like” contrast affects the visualization of ligaments and fibrocartilaginous tissue that are directly visible on UTE and ZTE MRI. Moreover, synthetic images created using GRE sequences do not maintain the linear correlation with CT’s Hounsfield units as on UTE/ZTE. Nevertheless, as observed in this review, GRE-based synthetic CT has a high intermodality agreement with CT in assessing glenohumeral fractures, femoroacetabular impingement, lumbar spine degeneration, spinal and fractures[109].

SWI MRI showed promising results, and more studies from different centers and on 3T field strength scanners may confirm its robustness. The main challenges of SWI MRI are artifacts created by the high susceptibility around metal or air and the phase shifts in the interfaces between trabecular and bone marrow, amplified on 3T or 7T field strengths, decreasing its diagnostic performance.

Deep learning techniques are continuously developing, and new algorithms quickly emerge. U-net and GANs are currently the best-performing architectures for creating synthetic CT images, and many studies confirm their validity showing high morphological agreement with CT. The challenges of deep learning, and AI in general, include standardizing frameworks using different input images to obtain more homogeneous results across various sites.

MRI with a “CT-like” contrast can reduce the radiation exposure and, thus, the risk of radiation-induced neoplasia. Specifically, pediatric patients or those requiring repeated CT examinations, such as oncologic or sports medicine patients, can benefit the most from this new technology. In addition to generating highly similar images with CT, synthetic CT MRI can facilitate the co-registration of anatomic structures with T1-weighted and T2-weighted sequences, something not always easy with a CT examination usually performed at a different time and with the patient in a different position.

In conclusion, considering the results of the studies in this systematic review, synthetic CT can replace CT in some specific clinical diagnostics such as glenohumeral or spinal fractures, neuroforaminal stenosis, femoroacetabular impingement, temporomandibular joint degeneration, jaw osteonecrosis, bone erosions from inflammatory arthritis and bone tumors, osteolytic bone lesions, subacromial spurs, periarticular heterotopic ossifications, or spinal longitudinal ligament ossifications. It can also facilitate the diagnosis of soft tissue impingement or entrapment within bone fragments in complex fractures, often missed on CT examinations due to the better co-registration with other MRI sequences. It can also give quantitative compositional information such as bone porosity, bound or pore water

concentration, and T1 or T2* relaxation times. In oncologic patients, the linear correlation of signals from synthetic CT images and CT's Hounsfield units can be used for radiotherapy dose planning, MRI-only radiotherapy, and PET attenuation correction. The generation of synthetic CT images using MRI is an exciting and fast-growing field with many research and clinical applications and significant impacts on musculoskeletal disorders.

Supplementary Material

Refer to Web version on PubMed Central for supplementary material.

References

1. Amis ES Jr., Butler PF, Applegate KE, et al. American College of Radiology white paper on radiation dose in medicine. J Am Coll Radiol 2007;4(5):272–284. [PubMed: 17467608]
2. National Cancer Institute. Radiation Risks and Pediatric Computed Tomography (CT): A Guide for Health Care Providers 2018. Available at: https://wwwcancergov/about-cancer/causes-prevention/risk/radiation/pediatric-ct-scans. Accessed January 6, 2022.
3. US Food and Drug Administration. What are the Radiation Risks from CT? 2017. Available at: https://citationsycom/styles/investigative-radiology. Accessed January 6, 2022.
4. Fritz J. Automated and radiation-free generation of synthetic CT from MRI data: does AI help to cross the finish line? In. Vol 298: Radiological Society of North America; 2021:350–352.
5. Chang EY, Du J, Chung CB. UTE imaging in the musculoskeletal system. J Magn Reson Imaging 2015;41(4):870–883. [PubMed: 25045018]
6. Reichert IL, Robson MD, Gatehouse PD, et al. Magnetic resonance imaging of cortical bone with ultrashort TE pulse sequences. Magnetic resonance imaging 2005;23(5):611–618. [PubMed: 16051035]
7. Chen J, Chang EY, Carl M, et al. Measurement of bound and pore water T(1) relaxation times in cortical bone using three-dimensional ultrashort echo time cones sequences. Magn Reson Med 2017;77(6):2136–2145. [PubMed: 27263994]
8. Robson MD, Gatehouse PD, Bydder M, Bydder GM. Magnetic resonance: an introduction to ultrashort TE (UTE) imaging. J Comput Assist Tomogr 2003;27(6):825–846. [PubMed: 14600447]
9. Weiger M, Pruessmann KP, Hennel F. MRI with zero echo time: hard versus sweep pulse excitation. Magn Reson Med 2011;66(2):379–389. [PubMed: 21381099]
10. Ljungberg E, Damestani NL, Wood TC, et al. Silent zero TE MR neuroimaging: Current state-of-the-art and future directions. Progress in Nuclear Magnetic Resonance Spectroscopy 2021;123:73–93. [PubMed: 34078538]
11. Du J, Carl M, Bydder M, Takahashi A, Chung CB, Bydder GM. Qualitative and quantitative ultrashort echo time (UTE) imaging of cortical bone. Journal of Magnetic Resonance 2010;207(2):304–311. [PubMed: 20980179]
12. Li S, Chang EY, Bae WC, et al. Ultrashort echo time bi-component analysis of cortical bone—a field dependence study. Magnetic resonance in medicine 2014;71(3):1075–1081. [PubMed: 23630048]
13. Weiger M, Pruessmann K. MRI with zero echo time. eMagRes 2007.
14. Leynes AP, Larson PEZ. Synthetic CT Generation Using MRI with Deep Learning: How Does the Selection of Input Images Affect the Resulting Synthetic CT? Paper presented at: 2018 IEEE International Conference on Acoustics, Speech and Signal Processing (ICASSP); 15–20 April 2018, 2018.
15. Florkow MC, Zijlstra F, Willemsen K, et al. Deep learning–based MR-to-CT synthesis: The influence of varying gradient echo–based MR images as input channels. Magnetic resonance in medicine 2020;83(4):1429–1441. [PubMed: 31593328]
16. Tustison NJ, Avants BB, Cook PA, et al. N4ITK: improved N3 bias correction. IEEE Trans Med Imaging 2010;29(6):1310–1320. [PubMed: 20378467]

17. Khodarahmi I, Fritz J. The Value of 3 Tesla Field Strength for Musculoskeletal Magnetic Resonance Imaging. Invest Radiol 2021;56(11):749–763. [PubMed: 34190717]
18. Page MJ, McKenzie JE, Bossuyt PM, et al. The PRISMA 2020 statement: an updated guideline for reporting systematic reviews. BMJ 2021;372:n71. [PubMed: 33782057]
19. Lucas N, Macaskill P, Irwig L, et al. The reliability of a quality appraisal tool for studies of diagnostic reliability (QAREL). BMC Medical Research Methodology 2013;13(1):111. [PubMed: 24010406]
20. Gurney PT, Hargreaves BA, Nishimura DG. Design and analysis of a practical 3D cones trajectory. Magnetic Resonance in Medicine 2006;55(3):575–582. [PubMed: 16450366]
21. Bydder M, Carl M, Bydder GM, Du J. MRI chemical shift artifact produced by center-out radial sampling of k-space: a potential pitfall in clinical diagnosis. Quantitative Imaging in Medicine and Surgery 2021;11(8):3677–3683. [PubMed: 34341741]
22. Pauly J, Conolly S, Macovski A. Suppression of long T2 components for short T2 imaging. J Magn Reson Imaging 1992;2:145.
23. Gatehouse P, Bydder G. Magnetic resonance imaging of short T2 components in tissue. Clinical radiology 2003;58(1):1–19. [PubMed: 12565203]
24. Du J, Bydder M, Takahashi AM, Carl M, Chung CB, Bydder GM. Short T2 contrast with three-dimensional ultrashort echo time imaging. Magnetic Resonance Imaging 2011;29(4):470–482. [PubMed: 21440400]
25. Larson PEZ, Conolly SM, Pauly JM, Nishimura DG. Using adiabatic inversion pulses for long-T2 suppression in ultrashort echo time (UTE) imaging. Magnetic Resonance in Medicine 2007;58(5):952–961. [PubMed: 17969119]
26. Du J, Takahashi AM, Bae WC, Chung CB, Bydder GM. Dual inversion recovery, ultrashort echo time (DIR UTE) imaging: creating high contrast for short-T(2) species. Magn Reson Med 2010;63(2):447–455. [PubMed: 20099332]
27. Du J, Takahashi AM, Bydder M, Chung CB, Bydder GM. Ultrashort TE imaging with off-resonance saturation contrast (UTE-OSC). Magnetic Resonance in Medicine: An Official Journal of the International Society for Magnetic Resonance in Medicine 2009;62(2):527–531.
28. Carl M, Nazaran A, Bydder GM, Du J. Effects of fat saturation on short T2 quantification. Magn Reson Imaging 2017;43:6–9. [PubMed: 28629956]
29. Jang H, Carl M, Ma Y, et al. Fat suppression for ultrashort echo time imaging using a single-point Dixon method. NMR Biomed 2019;32(5):e4069. [PubMed: 30768813]
30. Horch RA, Nyman JS, Gochberg DF, Dortch RD, Does MD. Characterization of 1H NMR signal in human cortical bone for magnetic resonance imaging. Magnetic resonance in medicine 2010;64(3):680–687. [PubMed: 20806375]
31. Krug R, Larson PEZ, Wang C, et al. Ultrashort echo time MRI of cortical bone at 7 tesla field strength: a feasibility study. Journal of Magnetic Resonance Imaging 2011;34(3):691–695. [PubMed: 21769960]
32. Du J, Hermida JC, Diaz E, et al. Assessment of cortical bone with clinical and ultrashort echo time sequences. Magnetic Resonance in Medicine 2013;70(3):697–704. [PubMed: 23001864]
33. Nazaran A, Carl M, Ma Y, et al. Three-dimensional adiabatic inversion recovery prepared ultrashort echo time cones (3D IR-UTE-Cones) imaging of cortical bone in the hip. Magnetic Resonance Imaging 2017;44:60–64. [PubMed: 28716680]
34. Ma Y-j, West J, Nazaran A, et al. Feasibility of using an inversion-recovery ultrashort echo time (UTE) sequence for quantification of glenoid bone loss. Skeletal Radiology 2018;47(7):973–980. [PubMed: 29396694]
35. Finkenstaedt T, Siriwanarangsun P, Achar S, et al. Ultrashort Time-to-Echo Magnetic Resonance Imaging at 3 T for the Detection of Spondylolysis in Cadaveric Spines: Comparison With CT. Investigative Radiology 2019;54(1):32–38. [PubMed: 30157099]
36. Afsahi AM, Lombardi AF, Wei Z, et al. High-Contrast Lumbar Spinal Bone Imaging Using a 3D Slab-Selective UTE Sequence. Frontiers in Endocrinology 2022;12(1858).
37. Deininger-Czermak E, Villefort C, von Knebel Doeberitz N, et al. Comparison of MR ultrashort echo time and optimized 3D-multiecho in-phase sequence to computed tomography

for assessment of the osseous craniocervical junction. Journal of Magnetic Resonance Imaging 2021;53(4):1029–1039. [PubMed: 33368790]

38. Nguyen JC, Guariento A, Williams BA, et al. MRI evaluation of pediatric tibial eminence fractures: comparison between conventional and “CT-like” ultrashort echo time (UTE) images. Skeletal Radiology 2022:1–8.
39. Geiger D, Bae WC, Statum S, Du J, Chung CB. Quantitative 3D ultrashort time-to-echo (UTE) MRI and micro-CT (μCT) evaluation of the temporomandibular joint (TMJ) condylar morphology. Skeletal radiology 2014;43(1):19–25. [PubMed: 24092237]
40. Huber FA, Schumann P, Von Spiczak J, et al. Medication-Related osteonecrosis of the Jaw—Comparison of bone imaging using ultrashort Echo-Time magnetic resonance imaging and cone-beam computed tomography. Investigative radiology 2020;55(3):160–167. [PubMed: 31688157]
41. Du J, Carl M, Bydder M, Takahashi A, Chung CB, Bydder GM. Qualitative and quantitative ultrashort echo time (UTE) imaging of cortical bone. J Magn Reson 2010;207(2):304–311. [PubMed: 20980179]
42. Ma YJ, Lu X, Carl M, et al. Accurate T(1) mapping of short T(2) tissues using a three-dimensional ultrashort echo time cones actual flip angle imaging-variable repetition time (3D UTE-Cones AFI-VTR) method. Magn Reson Med 2018;80(2):598–608. [PubMed: 29314235]
43. Ma YJ, Zhao W, Wan L, et al. Whole knee joint T(1) values measured in vivo at 3T by combined 3D ultrashort echo time cones actual flip angle and variable flip angle methods. Magn Reson Med 2019;81(3):1634–1644. [PubMed: 30443925]
44. Reichert IL, Robson MD, Gatehouse PD, et al. Magnetic resonance imaging of cortical bone with ultrashort TE pulse sequences. Magn Reson Imaging 2005;23(5):611–618. [PubMed: 16051035]
45. Nazaran A, Carl M, Ma Y, et al. Three-dimensional adiabatic inversion recovery prepared ultrashort echo time cones (3D IR-UTE-Cones) imaging of cortical bone in the hip. Magn Reson Imaging 2017;44:60–64. [PubMed: 28716680]
46. Manhard MK, Horch RA, Gochberg DF, Nyman JS, Does MD. In vivo quantitative MR imaging of bound and pore water in cortical bone. Radiology 2015;277(1):221. [PubMed: 26020434]
47. Techawiboonwong A, Song HK, Leonard MB, Wehrli FW. Cortical bone water: in vivo quantification with ultrashort echo-time MR imaging. Radiology 2008;248(3):824–833. [PubMed: 18632530]
48. Horch RA, Gochberg DF, Nyman JS, Does MD. Clinically compatible MRI strategies for discriminating bound and pore water in cortical bone. Magnetic Resonance in Medicine 2012;68(6):1774–1784. [PubMed: 22294340]
49. Bae WC, Chen PC, Chung CB, Masuda K, D’Lima D, Du J. Quantitative ultrashort echo time (UTE) MRI of human cortical bone: correlation with porosity and biomechanical properties. J Bone Miner Res 2012;27(4):848–857. [PubMed: 22190232]
50. Jerban S, Lu X, Dorthe EW, et al. Correlations of cortical bone microstructural and mechanical properties with water proton fractions obtained from ultrashort echo time (UTE) MRI tricomponent T2* model. NMR in Biomedicine 2020;33(3):e4233. [PubMed: 31820518]
51. Rajapakse CS, Bashoor-Zadeh M, Li C, Sun W, Wright AC, Wehrli FW. Volumetric Cortical Bone Porosity Assessment with MR Imaging: Validation and Clinical Feasibility. Radiology 2015;276(2):526–535. [PubMed: 26203710]
52. Ma YJ, Chang EY, Carl M, Du J. Quantitative magnetization transfer ultrashort echo time imaging using a time-efficient 3D multispoke Cones sequence. Magn Reson Med 2018;79(2):692–700. [PubMed: 28470838]
53. Chang EY, Bae WC, Shao H, et al. Ultrashort echo time magnetization transfer (UTE-MT) imaging of cortical bone. NMR in Biomedicine 2015;28(7):873–880. [PubMed: 25981914]
54. Chen J, Carl M, Ma Y, et al. Fast volumetric imaging of bound and pore water in cortical bone using three-dimensional ultrashort-TE (UTE) and inversion recovery UTE sequences. NMR in Biomedicine 2016;29(10):1373–1380. [PubMed: 27496335]
55. Guo T, Ma Y, Jerban S, et al. T1 measurement of bound water in cortical bone using 3D adiabatic inversion recovery ultrashort echo time (3D IR-UTE) Cones imaging. Magnetic resonance in medicine 2020;84(2):634–645. [PubMed: 31863519]

56. Biswas R, Bae W, Diaz E, et al. Ultrashort echo time (UTE) imaging with bi-component analysis: bound and free water evaluation of bovine cortical bone subject to sequential drying. Bone 2012;50(3):749–755. [PubMed: 22178540]
57. Abbasi-Rad S, Saligheh Rad H. Quantification of Human Cortical Bone Bound and Free Water in Vivo with Ultrashort Echo Time MR Imaging: A Model-based Approach. Radiology 2017;283(3):862–872. [PubMed: 28051911]
58. Li C, Seifert AC, Rad HS, et al. Cortical bone water concentration: dependence of MR imaging measures on age and pore volume fraction. Radiology 2014;272(3):796. [PubMed: 24814179]
59. Hong AL, Ispiryan M, Padalkar MV, et al. MRI-derived bone porosity index correlates to bone composition and mechanical stiffness. Bone Rep 2019;11:100213. [PubMed: 31372372]
60. Jerban S, Ma Y, Wan L, et al. Collagen proton fraction from ultrashort echo time magnetization transfer (UTE-MT) MRI modelling correlates significantly with cortical bone porosity measured with micro-computed tomography (μCT). NMR Biomed 2019;32(2):e4045. [PubMed: 30549338]
61. Jerban S, Ma Y, Li L, et al. Volumetric mapping of bound and pore water as well as collagen protons in cortical bone using 3D ultrashort echo time cones MR imaging techniques. Bone 2019;127:120–128. [PubMed: 31176044]
62. Jerban S, Ma Y, Jang H, et al. Water proton density in human cortical bone obtained from ultrashort echo time (UTE) MRI predicts bone microstructural properties. Magnetic resonance imaging 2020;67:85–89. [PubMed: 31931112]
63. Jerban S, Ma Y, Dorthe EW, et al. Assessing cortical bone mechanical properties using collagen proton fraction from ultrashort echo time magnetization transfer (UTE-MT) MRI modeling. Bone reports 2019;11:100220. [PubMed: 31440531]
64. Jerban S, Ma Y, Nazaran A, et al. Detecting stress injury (fatigue fracture) in fibular cortical bone using quantitative ultrashort echo time-magnetization transfer (UTE-MT): an ex vivo study. NMR in Biomedicine 2018;31(11):e3994. [PubMed: 30059184]
65. Jerban S, Ma Y, Wong JH, et al. Ultrashort echo time magnetic resonance imaging (UTE-MRI) of cortical bone correlates well with histomorphometric assessment of bone microstructure. Bone 2019;123:8–17. [PubMed: 30877070]
66. Carl M, Bydder GM, Du J. UTE imaging with simultaneous water and fat signal suppression using a time-efficient multispoke inversion recovery pulse sequence. Magn Reson Med 2016;76(2):577–582. [PubMed: 26309221]
67. Breighner RE, Endo Y, Konin GP, Gulotta LV, Koff MF, Potter HG. Technical Developments: Zero Echo Time Imaging of the Shoulder: Enhanced Osseous Detail by Using MR Imaging. Radiology 2018;286(3):960–966. [PubMed: 29117482]
68. Hafner S Fast imaging in liquids and solids with the Back-projection Low Angle ShoT (BLAST) technique. Magnetic Resonance Imaging 1994;12(7):1047–1051. [PubMed: 7997092]
69. Madio DP, Lowe IJ. Ultra-fast imaging using low flip angles and fids. Magnetic Resonance in Medicine 1995;34(4):525–529. [PubMed: 8524019]
70. Schulte RF, Buonincontri G, Costagli M, Menini A, Wiesinger F, Solana AB. Silent T2* and T2 encoding using ZTE combined with BURST. Magnetic Resonance in Medicine 2019;81(4):2277–2287. [PubMed: 30387897]
71. Wiesinger F, Menini A, Solana AB. Looping Star. Magn Reson Med 2019;81(1):57–68. [PubMed: 30106186]
72. Ljungberg E, Wood T, Solana AB, et al. Silent T1 mapping using the variable flip angle method with B1 correction. Magnetic Resonance in Medicine 2020;84(2):813–824. [PubMed: 31961961]
73. Matsuo-Hagiyama C, Watanabe Y, Tanaka H, et al. Comparison of Silent and Conventional MR Imaging for the Evaluation of Myelination in Children. Magnetic Resonance in Medical Sciences 2017;16(3):209–216. [PubMed: 27795484]
74. Yuan J, Hu Y, Menini A, et al. Near-silent distortionless DWI using magnetization-prepared RUFIS. Magnetic Resonance in Medicine 2020;84(1):170–181. [PubMed: 31782557]
75. Kuethe DO, Caprihan A, Lowe IJ, Madio DP, Gach HM. Transforming NMR data despite missing points. J Magn Reson 1999;139(1):18–25. [PubMed: 10388580]
76. Wu Y, Dai G, Ackerman JL, et al. Water- and fat-suppressed proton projection MRI (WASPI) of rat femur bone. Magn Reson Med 2007;57(3):554–567. [PubMed: 17326184]

77. Grodzki DM, Jakob PM, Heismann B. Ultrashort echo time imaging using pointwise encoding time reduction with radial acquisition (PETRA). Magn Reson Med 2012;67(2):510–518. [PubMed: 21721039]

78. Froidevaux R, Weiger M, Rösler MB, Brunner DO, Pruessmann KP. HYFI: Hybrid filling of the dead-time gap for faster zero echo time imaging. NMR Biomed 2021;34(6):e4493. [PubMed: 33624305]

79. Grodzki DM, Jakob PM, Heismann B. Correcting slice selectivity in hard pulse sequences. J Magn Reson 2012;214(1):61–67. [PubMed: 22047992]

80. Weiger M, Pruessmann KP. MRI with Zero Echo Time. In: eMagRes

81. Horch RA, Wilkens K, Gochberg DF, Does MD. RF coil considerations for short-T2 MRI. Magnetic Resonance in Medicine 2010;64(6):1652–1657. [PubMed: 20665825]

82. Engström M, McKinnon G, Cozzini C, Wiesinger F. In-phase zero TE musculoskeletal imaging. Magn Reson Med 2020;83(1):195–202. [PubMed: 31429994]

83. de Mello RAF, Ma Y-j, Ashir A, et al. Three-Dimensional Zero Echo Time Magnetic Resonance Imaging Versus 3-Dimensional Computed Tomography for Glenoid Bone Assessment. Arthroscopy: The Journal of Arthroscopic & Related Surgery 2020;36(9):2391–2400. [PubMed: 32502712]

84. Argentieri EC, Koff MF, Breighner RE, Endo Y, Shah PH, Sneag DB. Diagnostic Accuracy of Zero-Echo Time MRI for the Evaluation of Cervical Neural Foraminal Stenosis. Spine (Phila Pa 1976) 2018;43(13):928–933. [PubMed: 29095415]

85. Hou B, Liu C, Li Y, et al. Evaluation of the degenerative lumbar osseous morphology using zero echo time magnetic resonance imaging (ZTE-MRI). European Spine Journal 2022:1–9.

86. Li Y, Xiong Y, Hou B, et al. Comparison of zero echo time MRI with T1-weighted fast spin echo for the recognition of sacroiliac joint structural lesions using CT as the reference standard. European Radiology 2022:1–11.

87. Jeong HS, Park C, Kim KS, Kim JH, Jeon CH. Clinical feasibility of MR-generated synthetic CT images of the cervical spine: Diagnostic performance for detection of OPLL and comparison of CT number. Medicine (Baltimore) 2021;100(18):e25800. [PubMed: 33950980]

88. Ma YJ, Chang EY. Ossification of the Posterior Longitudinal Ligament on Zero-TE MRI With “CT-Like” Contrast. AJR Am J Roentgenol 2021;217(5):1242. [PubMed: 34076461]

89. Breighner RE, Bogner EA, Lee SC, Koff MF, Potter HG. Evaluation of Osseous Morphology of the Hip Using Zero Echo Time Magnetic Resonance Imaging. Am J Sports Med 2019;47(14):3460–3468. [PubMed: 31633993]

90. Amar R, Thiry T, Salga M, et al. Comparison of magnetic resonance imaging and computed tomography for bone assessment of neurogenic heterotopic ossification of the hip: a preliminary study. Journal of Orthopaedic Surgery and Research 2021;16(1):1–11. [PubMed: 33397415]

91. Bharadwaj UU, Coy A, Motamedi D, et al. CT-like MRI: a qualitative assessment of ZTE sequences for knee osseous abnormalities. Skeletal Radiology 2022:1–10.

92. Sandberg JK, Young VA, Yuan J, Hargreaves BA, Wishah F, Vasanawala SS. Zero echo time pediatric musculoskeletal magnetic resonance imaging: initial experience. Pediatr Radiol 2021;51(13):2549–2560. [PubMed: 34156504]

93. Lee C, Jeon KJ, Han SS, et al. CT-like MRI using the zero-TE technique for osseous changes of the TMJ. Dentomaxillofac Radiol 2020;49(3):20190272. [PubMed: 31670578]

94. Yuan J, Hu Y, Menini A, et al. Near-silent distortionless DWI using magnetization-prepared RUFIS. Magn Reson Med 2020;84(1):170–181. [PubMed: 31782557]

95. Sandberg JK, Young VA, Syed AB, et al. Near-Silent and Distortion-Free Diffusion MRI in Pediatric Musculoskeletal Disorders: Comparison With Echo Planar Imaging Diffusion. J Magn Reson Imaging 2021;53(2):504–513. [PubMed: 32815203]

96. Larson PE, Han M, Krug R, et al. Ultrashort echo time and zero echo time MRI at 7T. Magma 2016;29(3):359–370. [PubMed: 26702940]

97. Koh E, Walton ER, Watson P. VIBE MRI: an alternative to CT in the imaging of sports-related osseous pathology? The British Journal of Radiology 2018;91(1088):20170815. [PubMed: 29474097]

98. Johnson B, Alizai H, Dempsey M. Fast field echo resembling a CT using restricted echo-spacing (FRACTURE): a novel MRI technique with superior bone contrast. Skeletal Radiol 2021;50(8):1705–1713. [PubMed: 33175183]

99. Chong LR, Lee K, Sim FY. 3D MRI with CT-like bone contrast - An overview of current approaches and practical clinical implementation. Eur J Radiol 2021;143:109915. [PubMed: 34461599]

100. Gyftopoulos S, Yemin A, Mulholland T, et al. 3DMR osseous reconstructions of the shoulder using a gradient-echo based two-point Dixon reconstruction: a feasibility study. Skeletal Radiol 2013;42(3):347–352. [PubMed: 22829026]

101. Gyftopoulos S, Beltran LS, Yemin A, et al. Use of 3D MR reconstructions in the evaluation of glenoid bone loss: a clinical study. Skeletal Radiol 2014;43(2):213–218. [PubMed: 24318071]

102. Lansdown DA, Cvetanovich GL, Verma NN, et al. Automated 3-Dimensional Magnetic Resonance Imaging Allows for Accurate Evaluation of Glenoid Bone Loss Compared With 3-Dimensional Computed Tomography. Arthroscopy 2019;35(3):734–740. [PubMed: 30733040]

103. Stillwater L, Koenig J, Maycher B, Davidson M. 3D-MR vs. 3D-CT of the shoulder in patients with glenohumeral instability. Skeletal Radiol 2017;46(3):325–331. [PubMed: 28028575]

104. Samim M, Eftekhary N, Vigdorchik JM, et al. 3D-MRI versus 3D-CT in the evaluation of osseous anatomy in femoroacetabular impingement using Dixon 3D FLASH sequence. Skeletal Radiol 2019;48(3):429–436. [PubMed: 30182297]

105. Subramanian A, Hegde G, Azzopardi C, et al. TI VIBE inversion MRI - An alternative to CT for imaging of hip pain. J Clin Orthop Trauma 2021;19:196–199. [PubMed: 34123724]

106. Ang EC, Robertson AF, Malara FA, et al. Diagnostic accuracy of 3-T magnetic resonance imaging with 3D T1 VIBE versus computer tomography in pars stress fracture of the lumbar spine. Skeletal Radiol 2016;45(11):1533–1540. [PubMed: 27614965]

107. Gersing AS, Pfeiffer D, Kopp FK, et al. Evaluation of MR-derived CT-like images and simulated radiographs compared to conventional radiography in patients with benign and malignant bone tumors. Eur Radiol 2019;29(1):13–21. [PubMed: 29948069]

108. Deininger-Czermak E, Villefort C, von Knebel Doeberitz N, et al. Comparison of MR Ultrashort Echo Time and Optimized 3D-Multiecho In-Phase Sequence to Computed Tomography for Assessment of the Osseous Craniocervical Junction. J Magn Reson Imaging 2021;53(4):1029–1039. [PubMed: 33368790]

109. Schwaiger BJ, Schneider C, Kronthaler S, et al. CT-like images based on T1 spoiled gradient-echo and ultra-short echo time MRI sequences for the assessment of vertebral fractures and degenerative bone changes of the spine. European Radiology 2021;31(7):4680–4689. [PubMed: 33443599]

110. Schwaiger BJ, Schneider C, Kronthaler S, et al. CT-like images based on T1 spoiled gradient-echo and ultra-short echo time MRI sequences for the assessment of vertebral fractures and degenerative bone changes of the spine. Eur Radiol 2021;31(7):4680–4689. [PubMed: 33443599]

111. Haacke EM, Xu Y, Cheng Y-CN, Reichenbach JR. Susceptibility weighted imaging (SWI). Magnetic Resonance in Medicine 2004;52(3):612–618. [PubMed: 15334582]

112. Ulas ST, Ziegeler K, Richter S-T, et al. CT-like images in MRI improve specificity of erosion detection in patients with hand arthritis: a diagnostic accuracy study with CT as standard of reference. RMD open 2022;8(1):e002089. [PubMed: 35177555]

113. Engel G, Bender YY, Adams LC, et al. Evaluation of osseous cervical foraminal stenosis in spinal radiculopathy using susceptibility-weighted magnetic resonance imaging. Eur Radiol 2019;29(4):1855–1862. [PubMed: 30324384]

114. Böker SM, Adams LC, Bender YY, et al. Differentiation of Predominantly Osteoblastic and Osteolytic Spine Metastases by Using Susceptibility-weighted MRI. Radiology 2019;290(1):146–154. [PubMed: 30375926]

115. Böker SM, Bender YY, Adams LC, et al. Evaluation of sclerosis in Modic changes of the spine using susceptibility-weighted magnetic resonance imaging. European Journal of Radiology 2017;88:148–154. [PubMed: 28189200]

116. Böker SM, Adams LC, Bender YY, et al. Evaluation of vertebral body fractures using susceptibility-weighted magnetic resonance imaging. Eur Radiol 2018;28(5):2228–2235. [PubMed: 29260364]
117. Nörenberg D, Armbruster M, Bender YN, et al. Diagnostic performance of susceptibility-weighted magnetic resonance imaging for the assessment of sub-coracoacromial spurs causing subacromial impingement syndrome. Eur Radiol 2017;27(3):1286–1294. [PubMed: 27287483]
118. Bender YY, Diederichs G, Walter TC, et al. Differentiation of Osteophytes and Disc Herniations in Spinal Radiculopathy Using Susceptibility-Weighted Magnetic Resonance Imaging. Invest Radiol 2017;52(2):75–80. [PubMed: 27548342]
119. Böker SM, Adams LC, Fahlenkamp UL, Diederichs G, Hamm B, Makowski MR. Value of susceptibility-weighted imaging for the assessment of angle measurements reflecting hip morphology. Scientific Reports 2020;10(1):20899. [PubMed: 33262372]
120. Deppe D, Hermann KG, Proft F, et al. CT-like images of the sacroiliac joint generated from MRI using susceptibility-weighted imaging (SWI) in patients with axial spondyloarthritis. RMD Open 2021;7(2).
121. Shelhamer E, Long J, Darrell T. Fully Convolutional Networks for Semantic Segmentation. IEEE Transactions on Pattern Analysis and Machine Intelligence 2017;39(4):640–651. [PubMed: 27244717]
122. Goodfellow I, Pouget-Abadie J, Mirza M, et al. Generative adversarial nets. Advances in neural information processing systems 2014;27.
123. Emami H, Dong M, Nejad-Davarani SP, Glide-Hurst CK. Generating synthetic CTs from magnetic resonance images using generative adversarial networks. Med Phys 2018.
124. Florkow MC, Zijlstra F, Willemsen K, et al. Deep learning-based MR-to-CT synthesis: The influence of varying gradient echo-based MR images as input channels. Magn Reson Med 2020;83(4):1429–1441. [PubMed: 31593328]
125. Leynes AP, Larson PE. Synthetic CT Generation using MRI with Deep Learning: How does the selection of input images affect the resulting synthetic CT? Paper presented at: 2018 IEEE International Conference on Acoustics, Speech and Signal Processing (ICASSP)2018.
126. Wang T, Lei Y, Fu Y, et al. A review on medical imaging synthesis using deep learning and its clinical applications. Journal of applied clinical medical physics 2021;22(1):11–36.
127. Johnstone E, Wyatt JJ, Henry AM, et al. Systematic review of synthetic computed tomography generation methodologies for use in magnetic resonance imaging–only radiation therapy. International Journal of Radiation Oncology* Biology* Physics 2018;100(1):199–217.
128. Florkow MC, Willemsen K, Zijlstra F, et al. MRI-based synthetic CT shows equivalence to conventional CT for the morphological assessment of the hip joint. J Orthop Res 2021.
129. Staartjes VE, Seevinck PR, Vandertop WP, van Stralen M, Schröder ML. Magnetic resonance imaging-based synthetic computed tomography of the lumbar spine for surgical planning: a clinical proof-of-concept. Neurosurg Focus 2021;50(1):E13.
130. Morbée L, Chen M, Herregods N, Pullens P, Jans LBO. MRI-based synthetic CT of the lumbar spine: Geometric measurements for surgery planning in comparison with CT. Eur J Radiol 2021;144:109999. [PubMed: 34700094]
131. Willemsen K, Ketel MHM, Zijlstra F, et al. 3D-printed saw guides for lower arm osteotomy, a comparison between a synthetic CT and CT-based workflow. 3D Print Med 2021;7(1):13. [PubMed: 33914209]
132. Jans LBO, Chen M, Elewaut D, et al. MRI-based Synthetic CT in the Detection of Structural Lesions in Patients with Suspected Sacroiliitis: Comparison with MRI. Radiology 2021;298(2):343–349. [PubMed: 33350891]
133. Lena B, Florkow MC, Ferrer CJ, et al. Synthetic CT for the planning of MR-HIFU treatment of bone metastases in pelvic and femoral bones: a feasibility study. European Radiology 2022:1–10.
134. McCalden RW, McGeough JA, Barker MB, Court-Brown CM. Age-related changes in the tensile properties of cortical bone. The relative importance of changes in porosity, mineralization, and microstructure. J Bone Joint Surg Am 1993;75(8):1193–1205. [PubMed: 8354678]

135. Schuit SC, van der Klift M, Weel AE, et al. Fracture incidence and association with bone mineral density in elderly men and women: the Rotterdam Study. Bone 2004;34(1):195–202. [PubMed: 14751578]

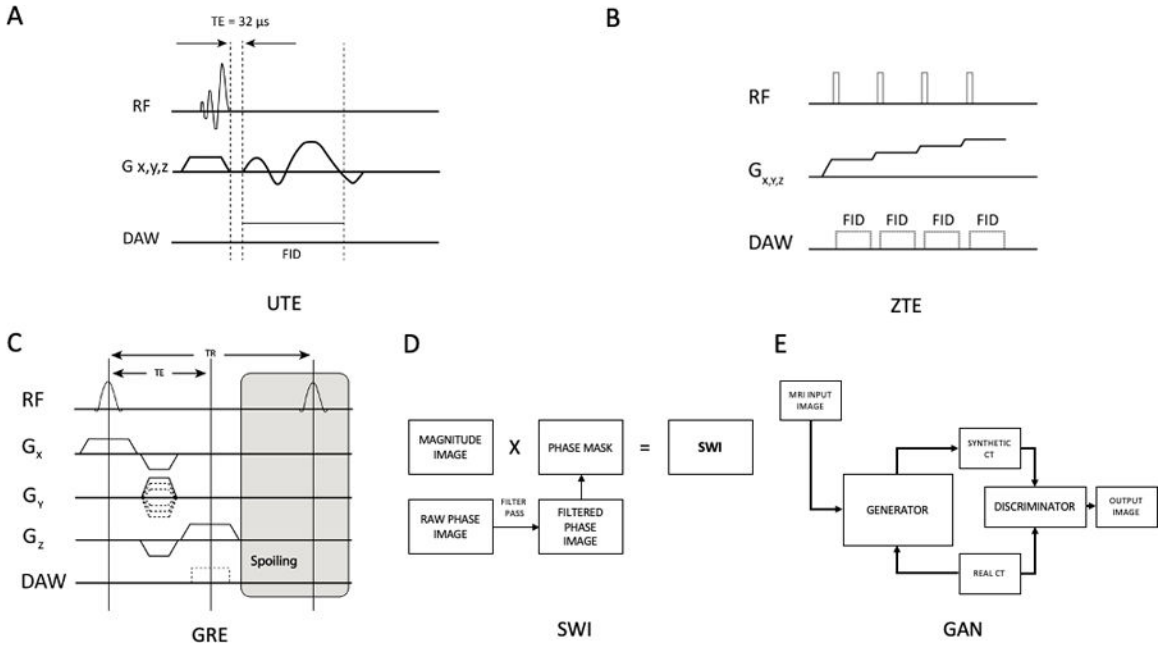

Figure 1.

Sequence diagrams of UTE Cones MRI sequence (A), ZTE MRI sequence (B), basic GRE MRI sequence (C), and schematic representations of synthetic CT image creation using SWI MRI (D), and GANs (E). UTE: ultra-short echo-time; ZTE: zero echo-time; GRE: gradient-echo; SWI: susceptibility-weighted imaging; GAN: generative adversarial networks.

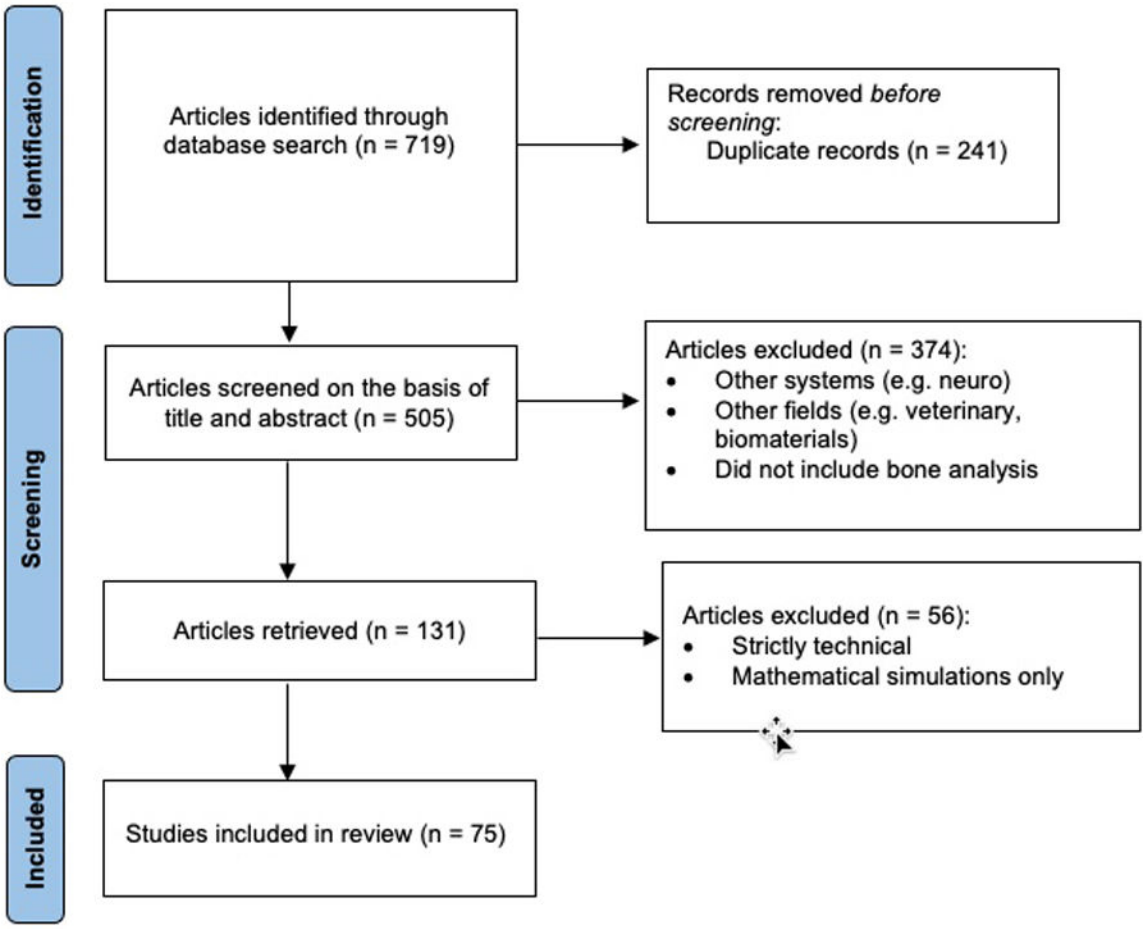

Figure 2.
PRISMA flowchart demonstrating the process for selection of studies.

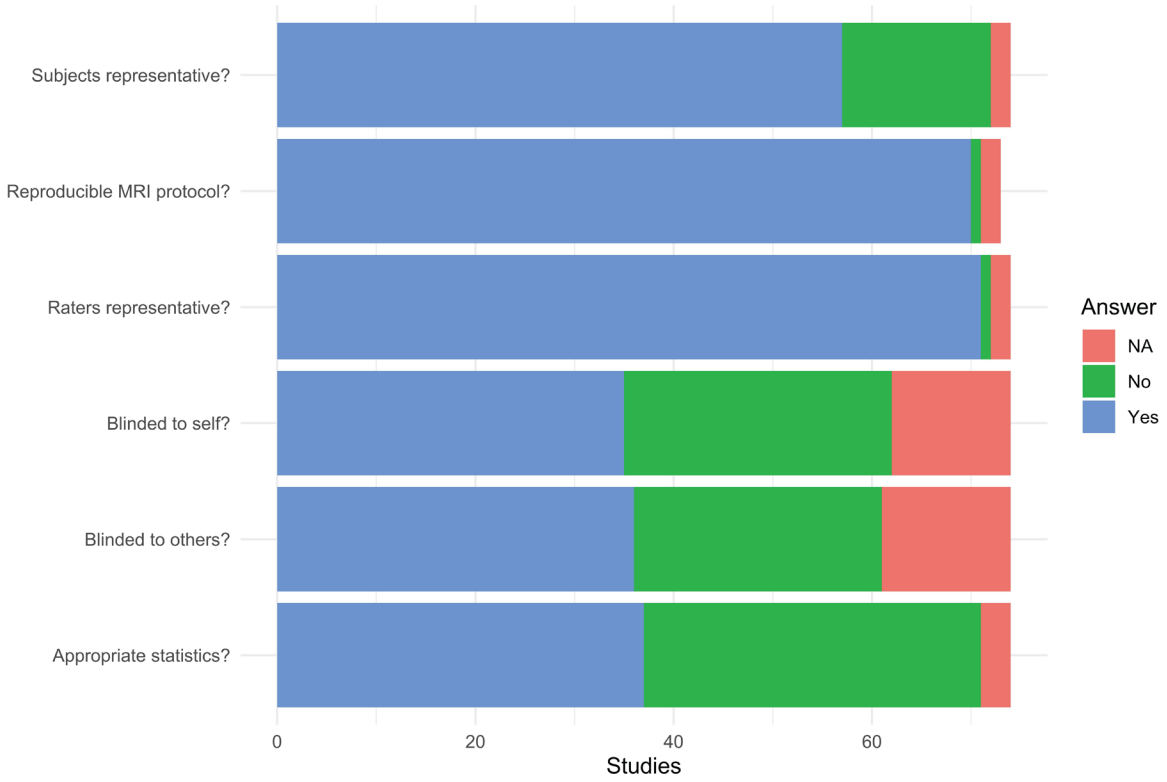

Figure 3.
Results of QAREL reliability assessment of individual studies

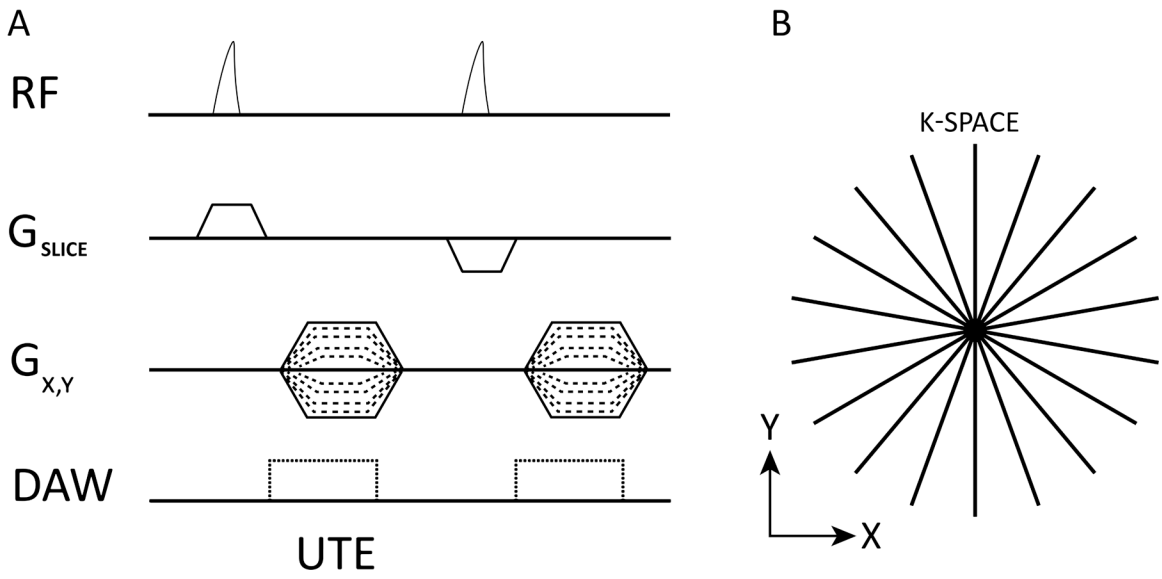

Figure 4.

The basic 2D UTE sequence diagram. A truncated RF pulse is applied together with a slice-selective gradient (A). After excitation, the spatial encoding gradient is turned on, and data acquisition begins with radial k-space sampling (B).

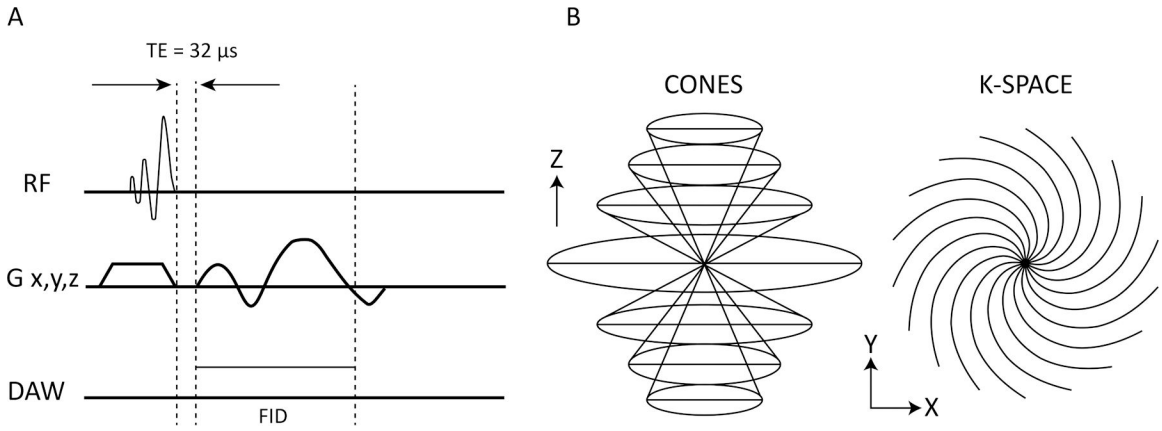

Figure 5.

The 3D UTE cones sequence diagram. A short slab-selective RF pulse is used for signal excitation (A), followed by a Cones trajectory k-space sampling.

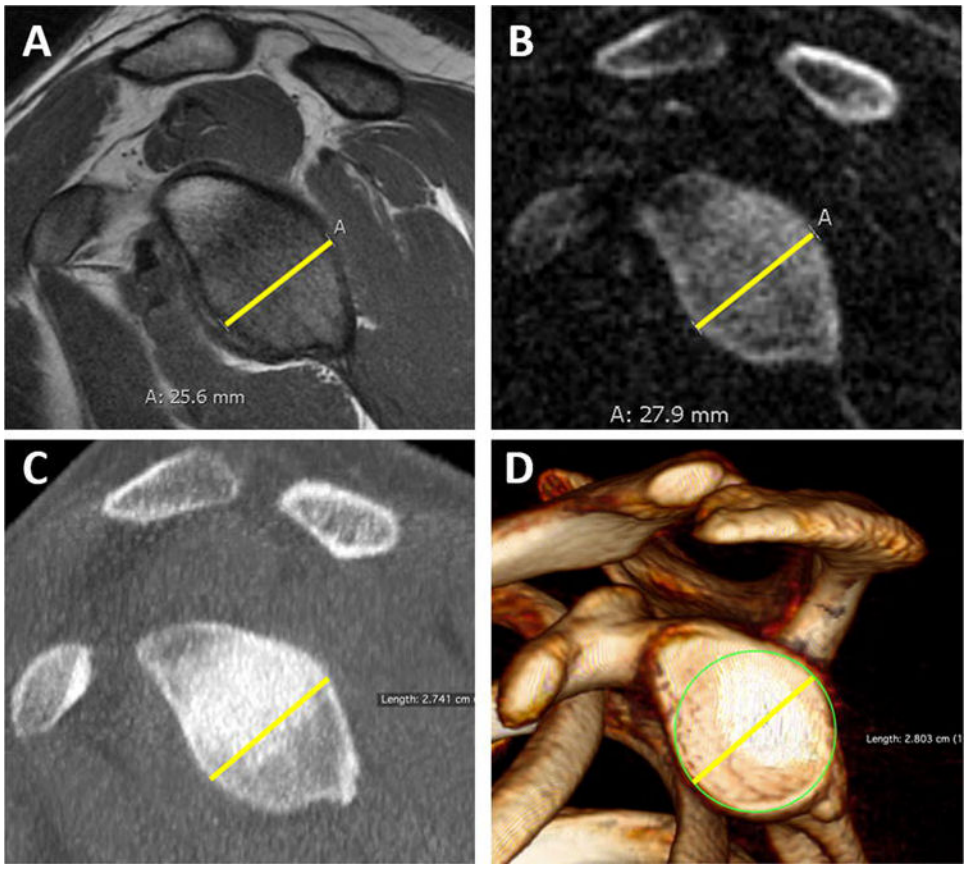

Figure 6.

30-year-old patient with glenohumeral instability. (A) T1-weighted image shows poor definition of glenoid cortical bone contour and measurement of 2.56 cm was obtained. (B) IR-UTE-Cones image shows excellent depiction of bone contours and measurement of 2.79 cm was obtained, which is nearly perfect when compared with 3D CT measurement. (C) 2D CT image also shows excellent depiction of contours with 2.74 cm glenoid diameter. (D) 3D CT image was used as the reference standard. This figure was previously presented by Ma et al[29] in "Feasibility of Using an Inversion-Recovery Ultrashort Echo Time (UTE) Sequence For Quantification of Glenoid Bone Loss – Springer Link". Reprinting permission granted through the Rightslink system.

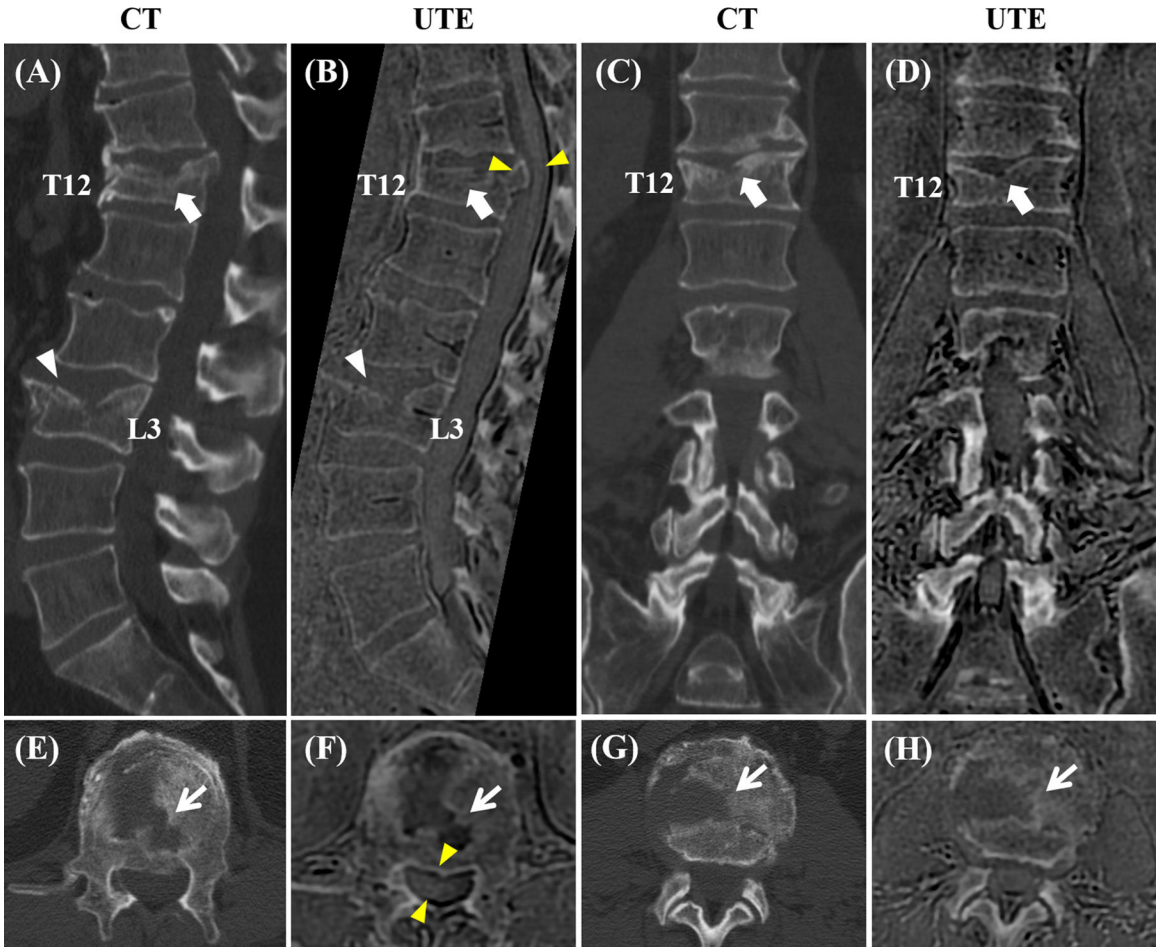

Figure 7.

Correlation between CT vs. 3D UTE MRI in a 72-year-old male with low back pain (T11-L5). Compression fractures are seen in T12 and L3 on the CT image (arrow and arrowhead in A, respectively) showing an excellent anatomic correlation with the 3D UTE MRI (arrow and arrowhead in B, respectively). Coronal (C and D) and axial (E-H) images also showed excellent anatomic correlation of the fractures between the CT scan and the 3D UTE MRI (arrows in E/F and G/H). Note the retropulsion of a bone fragment in T12 narrowing the spinal canal and its proximity to the spinal cord, which can be seen on the UTE sequence (yellow arrowheads in B and F). This figure was previously presented by Afsahi et al.[31]. *Reprinted from* "Frontiers | High-Contrast Lumbar Spinal Bone Imaging Using a 3D Slab-Selective UTE Sequence | Endocrinology (frontiersin.org)". *Licensed under CC BY 4.0.*

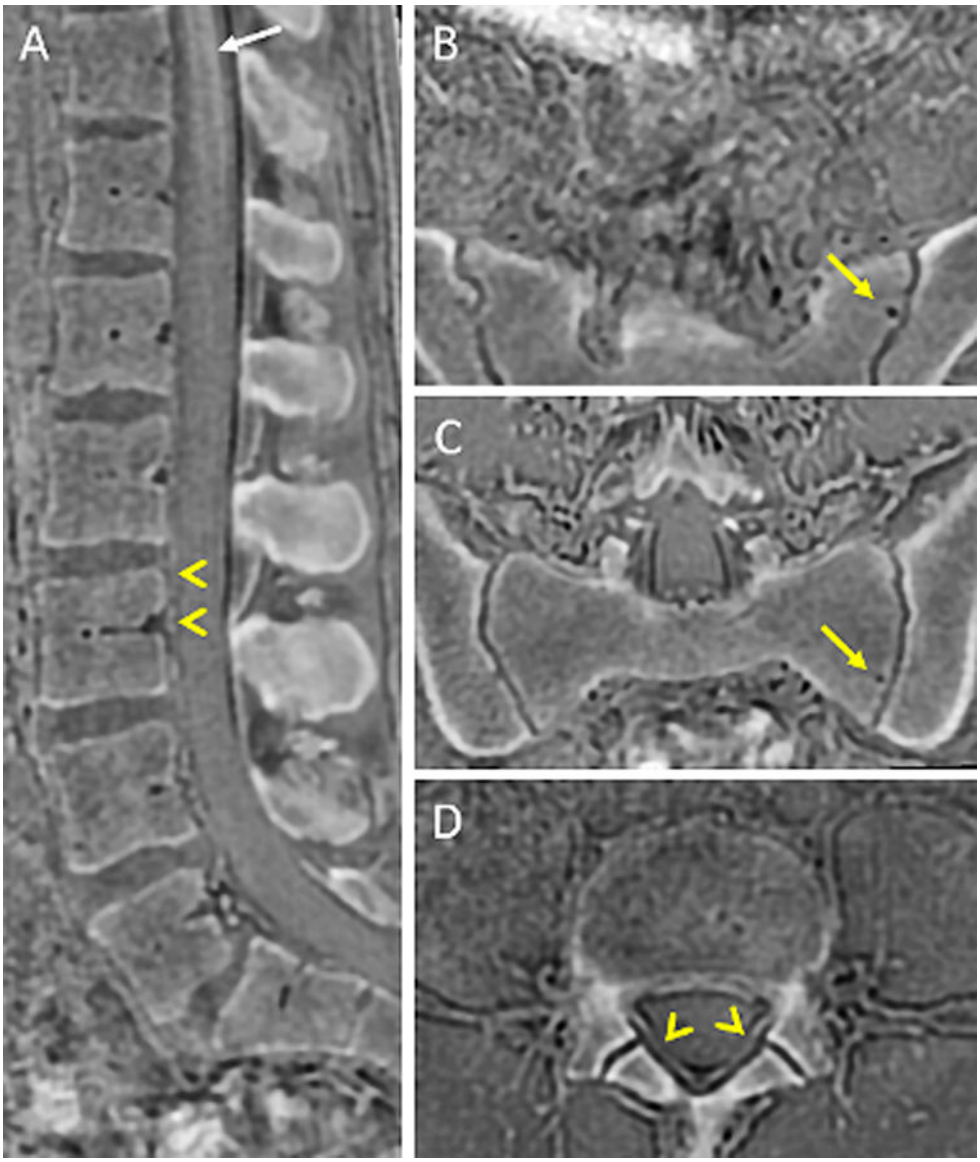

Figure 8.

3D slab selective UTE MRI of the lumbar spine from a 37-year-old male. The surrounding soft tissues, such as the anterior and posterior longitudinal ligaments and the ligamentum flavum (arrowheads in A and D), can be seen distinctly from the cortical bone. The high spatial resolution allows for evaluating small lesions such as subchondral cysts (yellow arrows in B and C). The slab selective radiofrequency pulse allows the “exclusion” of abdominal organs from the excitation, thus reducing the effects of respiratory artifacts.

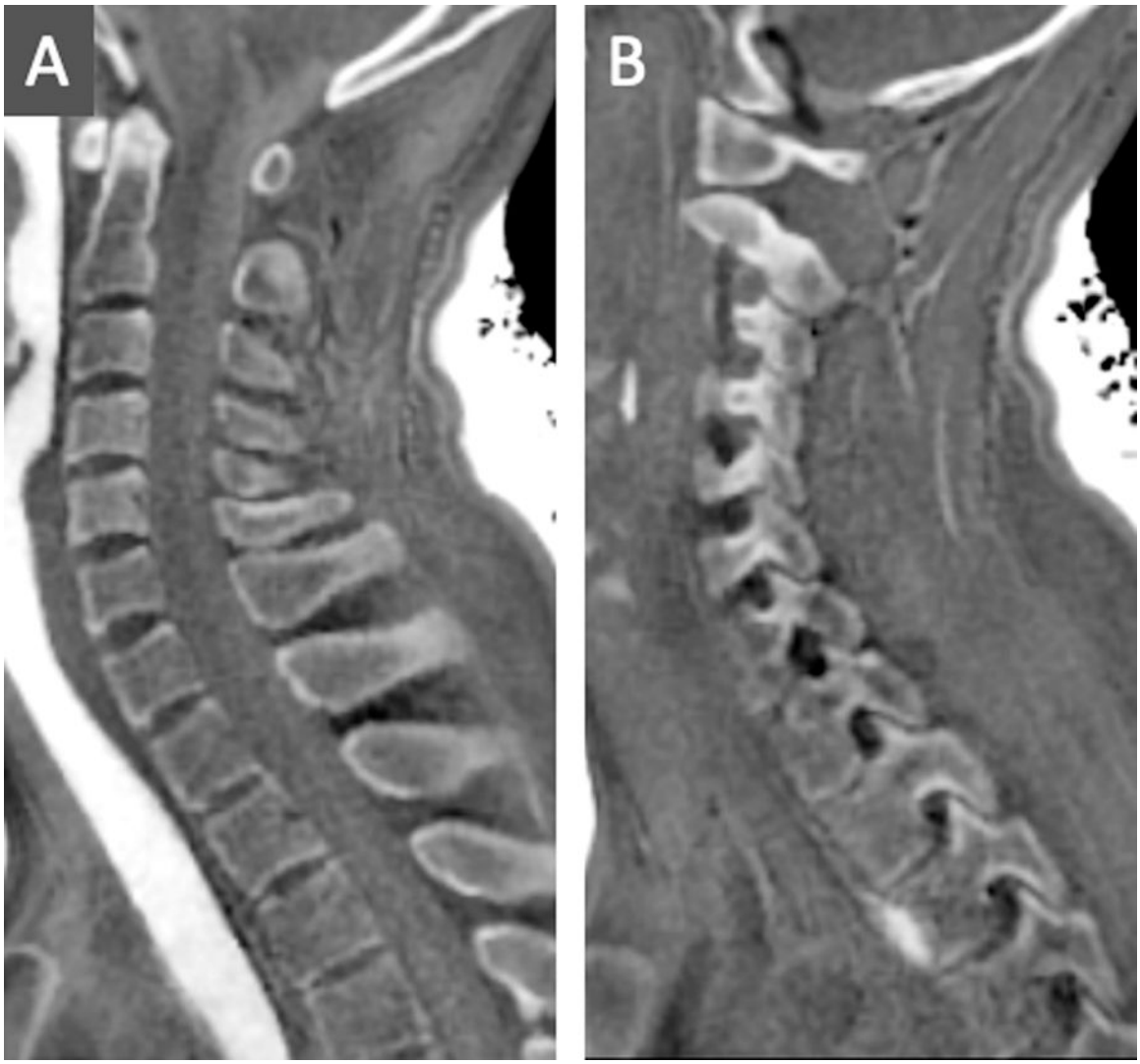

Figure 9.

Sagittal 3D slab-selective UTE MRI of an asymptomatic 28-year-old female shows the high definition of the vertebral body and spinal processes contours (A). The cervical neural foramina and facet joints are also depicted with high resolution and definition of its margins with a “CT-like” contrast (B). Slight image blurring is observed compared to images from Figure 8, possibly due to off-resonance artifacts.

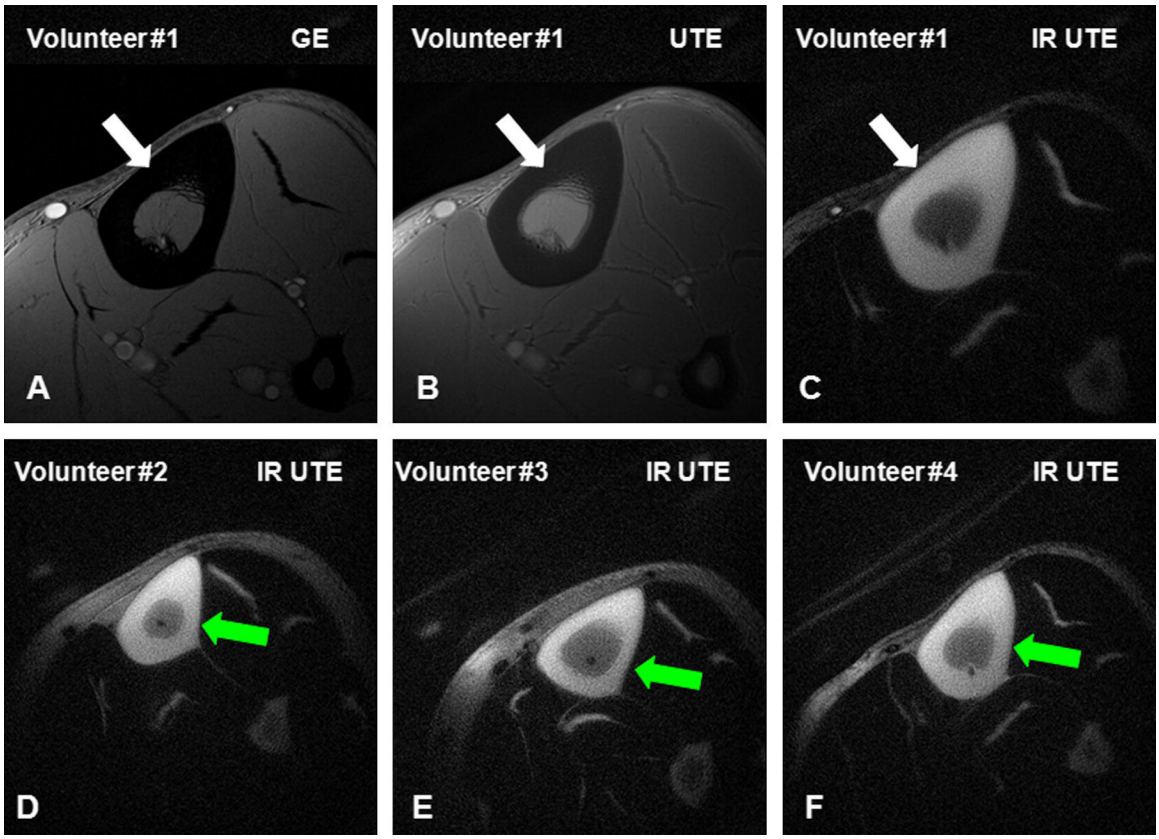

Figure 10.

The comparison of GRE, UTE, and IR-UTE sequences for imaging the tibia in human volunteers. Clinical GRE sequence shows pure signal void for the mid-diaphyseal tibia (arrow) (A). This is also low signal with UTE due to the high signal from the surrounding long T_2 muscle and fat (arrow) (B). The IR-UTE sequence shows consistent high contrast images for cortical bone of four healthy volunteers (C–F). Long T_2 muscle and fat signals were efficiently suppressed through adiabatic inversion and approximate signal nulling. This figure was previously presented by Du et al[6] in "Qualitative and quantitative ultrashort echo time (UTE) imaging of cortical bone - ScienceDirect". Reprinting permission granted through the Rightslink system.

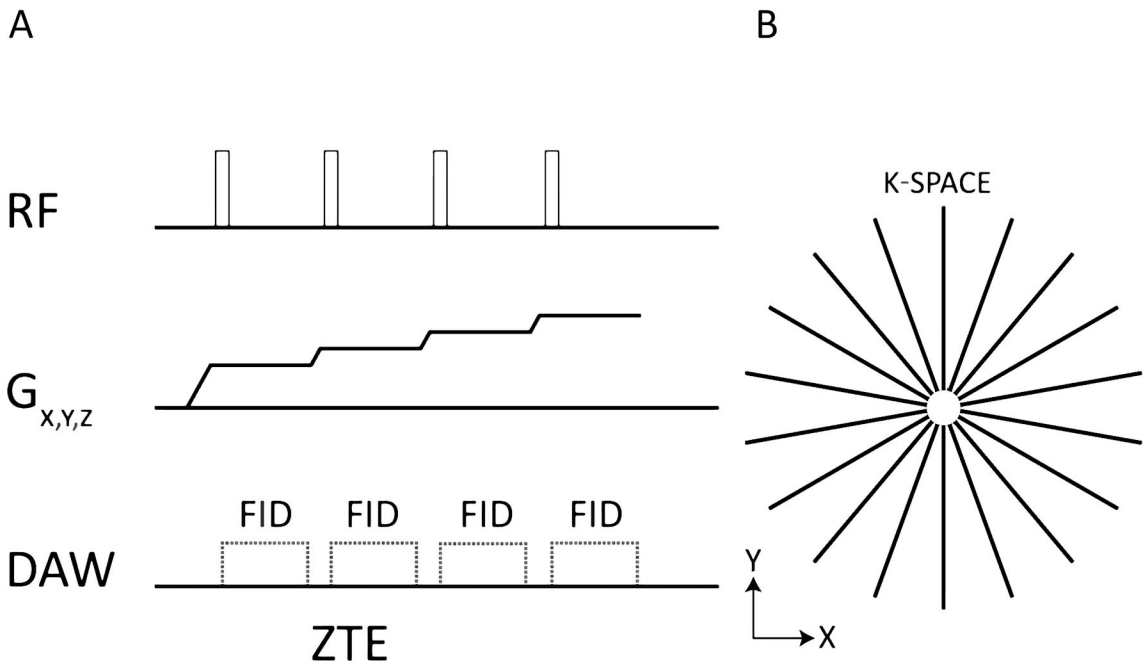

Figure 11.

The basic 3D ZTE sequence diagram. The ZTE sequence utilizes a non-selective rectangular RF pulse with a short duration for excitation (A), followed by a 3D center-out radial k-space sampling (B) with some missing data points at its center (white area in B). The readout gradients are turned on before signal excitation and evolve incrementally (Gx,y,z in A).

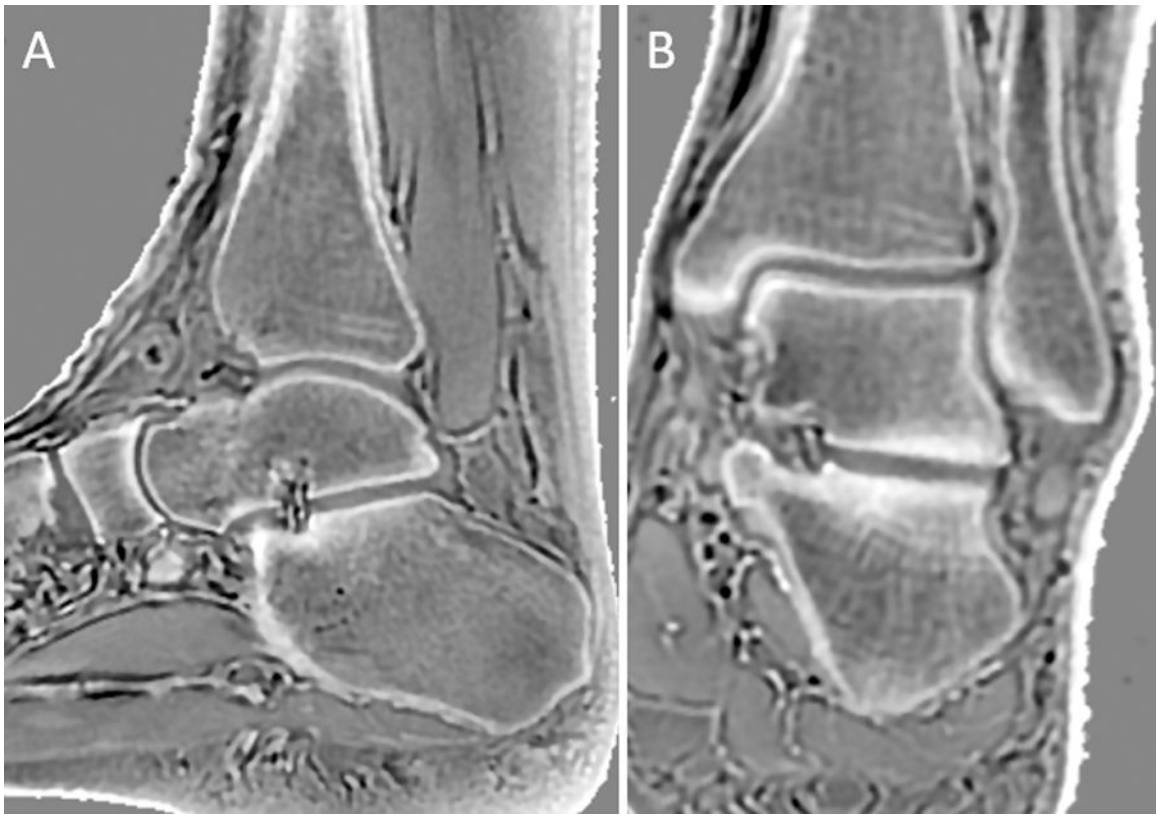

Figure 12.

Sagittal (A) and coronal (B) 3D ZTE MRI of the ankle from an asymptomatic 39-year-old male. Slice thickness = 1 mm, matrix size = 300 x 300, bandwidth = 73.2 KHz. The total scan time was 4 minutes.

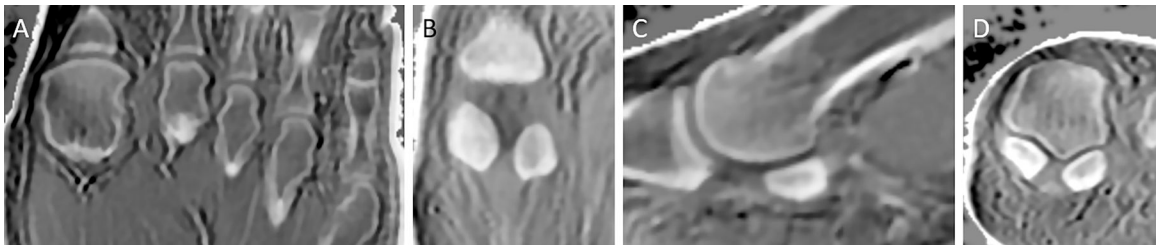

Figure 13.

Axial (A, B), sagittal (C), and coronal (D) 3D ZTE MRI at the metatarsophalangeal joints (A) and zoomed-in images of the metatarsophalangeal joint of the hallux (B, C, D) from an asymptomatic 39-year-old male. Cortical and trabecular bone can be seen with high resolution. Slice thickness = 1 mm, matrix size = 300 x 300, bandwidth = 73.2 KHz. The total scan time was 4 minutes.

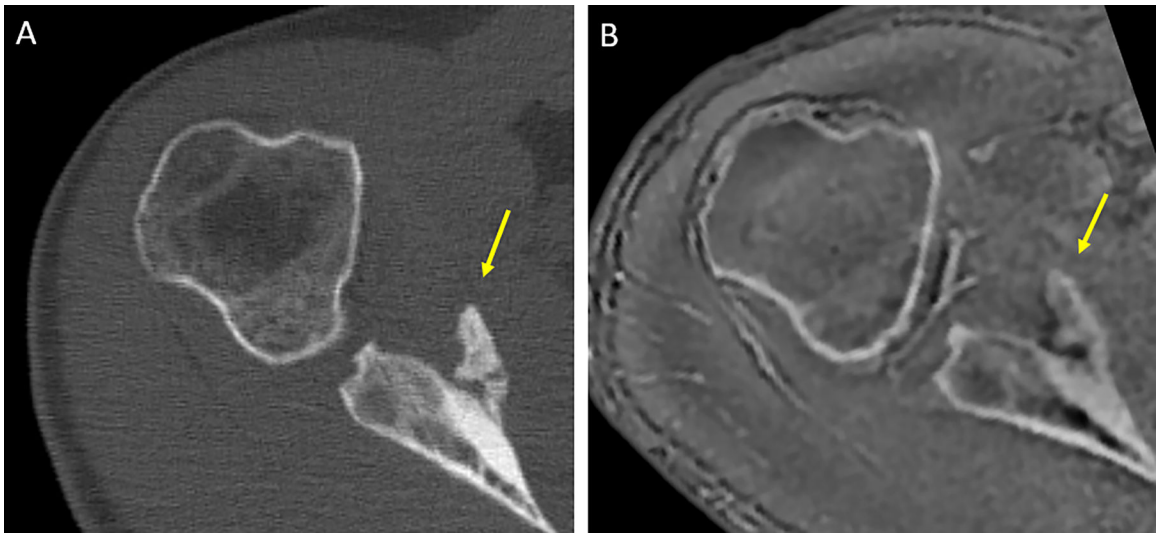

Figure 14.

Axial CT (A) and 3D ZTE MRI (B) from the right shoulder of a 40-year-old male presenting with glenohumeral instability symptoms show high intermodality agreement between CT and MRI. A dislocated bone fragment partially attached to the glenoid (Bony Bankart) is seen (yellow arrows) and corroborates the diagnosis of anterior shoulder dislocation.

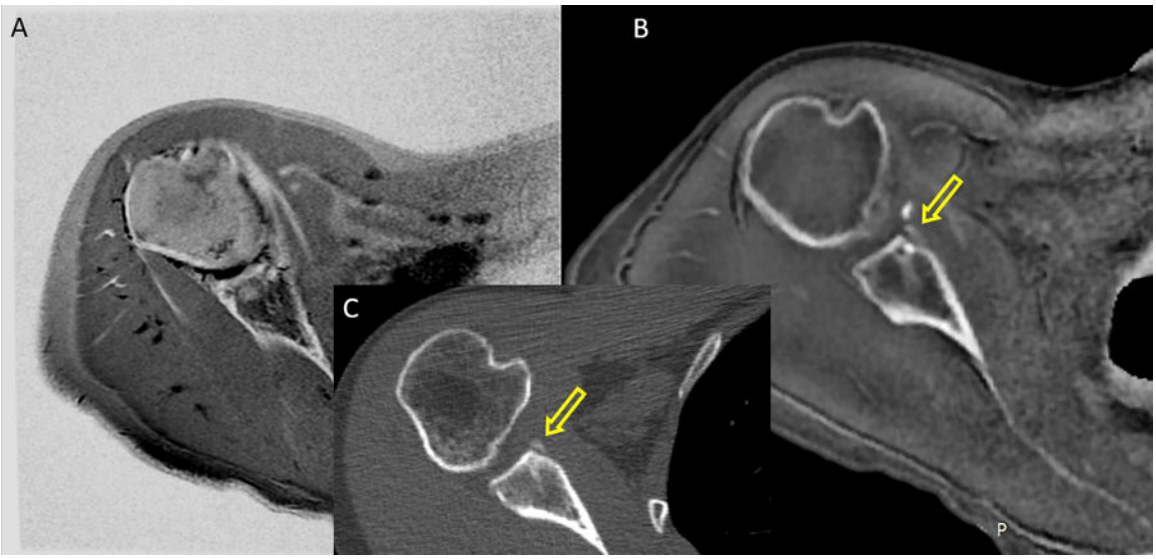

Figure 15.

Axial grayscale inverted images of an FSE T2-weighted MRI (A), axial 3D ZTE MRI (B), and axial CT (C) from the right shoulder of a 45-year-old male with glenohumeral joint instability. A bone fragment detached from the anteroinferior glenoid is easily detected on the ZTE MRI (arrow in B), and the CT images (arrow in C) compared to the FSE MRI.

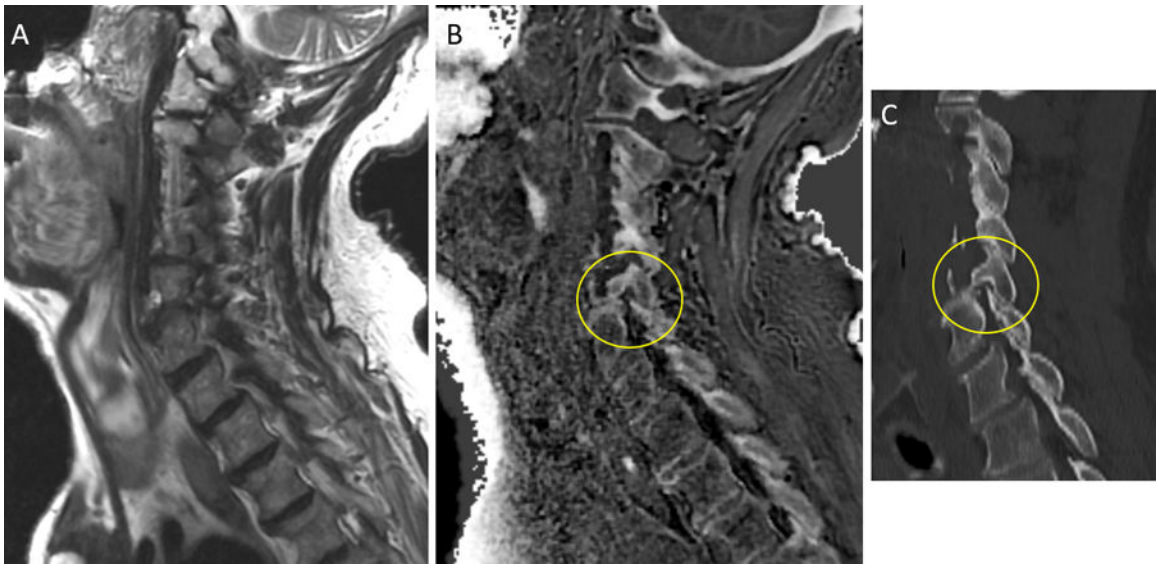

Figure 16.

Sagittal FSE T2-weighted MRI (A), 3D ZTE MRI (B), and CT (C) from the cervical spine of a 75-year-old male with cervical pain as well as myelopathy and radiculopathy symptoms. Note the neural foramen stenosis on ZTE MRI and CT (circled areas in B and C).

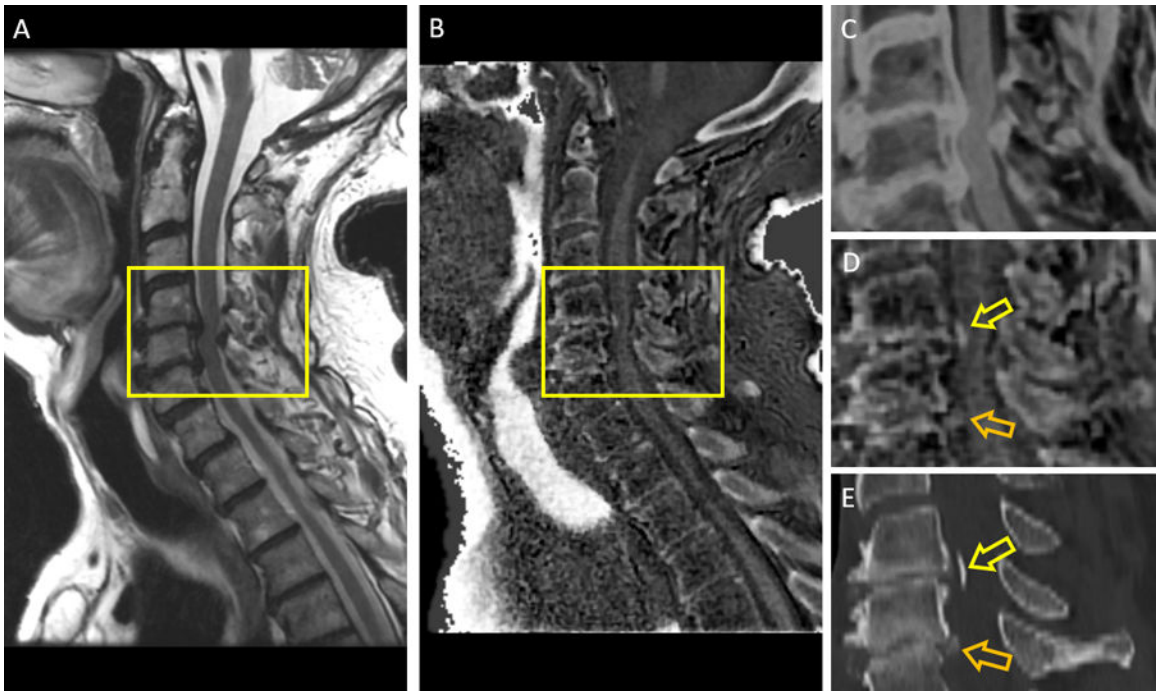

Figure 17.

Sagittal FSE T2-weighted MRI (A), sagittal 3D ZTE MRI (B), and zoomed-in images of the FSE T2-weighted MRI with grayscale inversion (C), 3D ZTE (D), and CT (E) from the cervical spine of the same 75-year-old male in Figure 13. Significant spinal canal stenosis is obvious, but ectopic ossifications and calcifications are not apparent on the FSE T2-weighted images (regular or inverted). However, the focus of posterior longitudinal ligament ossification at C4–5 (yellow arrows) and discal calcifications at C5–6 (orange arrows) are well-characterized on the ZTE image and confirmed on the CT.

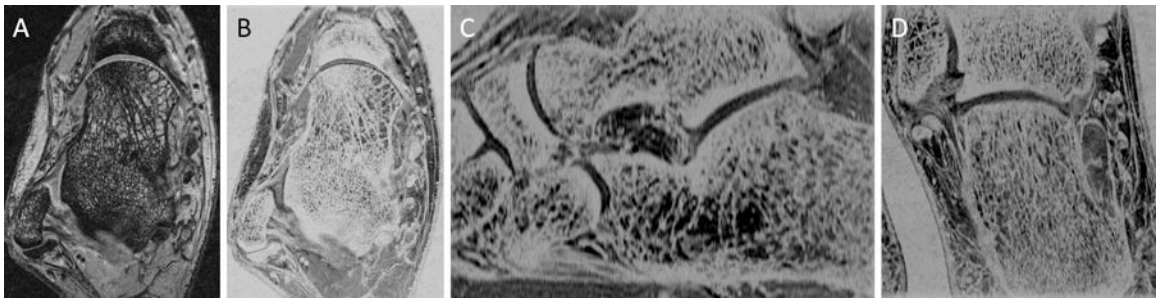

Figure 18.

3D GRE high-resolution sequence directed to the evaluation of trabecular bone of the talus and calcaneus from a 37-year-old male before (A) and after (B - D) image inversion to make cortical and trabecular bone bright. Matrix = 384 x 320, slice thickness = 1 mm, bandwidth = 18.24 KHz.

Table 1.

Characteristics of the studies included in the systematic review.

Study	Participants	Age	Female	Main Results	Field Strenght	MRI Sequence	Vendor	Scan Time	TR	TE	Matrix
Reichert (2005)	7 human subjects	54	3	• SNR = 10–70 • T1 = 140–260ms • T2* = 0.42–0.5ms	1.5T	2D-UTE dual subtraction/IR-UTE both with fat-suppression	Siemens	52s-8.5min	500ms	0.08, 2.87, 5.66, 8.45ms/0.08, 5.95, 11.08 and 17.70 ms	512x512
Du (2009)	• phantoms • 3 animal tissues • 5 human subjects			• CNR = 12–20 between short and long T2 tissues	3T	2D-UTE-OSC	GE		200–300ms	8μs	512
Du (2010)	• 1 human tissue • 5 human subjects	30	0	• SNR = 30 • CNR = 27 • T1 = 223±11ms • T2* = 390±19μs • %water = 23.3±1.6%	3T	2D-UTE dual echo subtraction/2D IR-UTE	GE	9min	300ms	8μs/4.4ms	512x512
Du (2011)	• 1 human subject • 7 human tissues	57	0	• High SNR/CNR between bone, fat, muscle with long T2 suppression	3T	3D-UTE dual echo subtraction/3D-IR-UTE/3D-DIR-UTE	GE	9–100min	15–300ms	8μs/2.2ms	256–384
Krug (2011)	• 5 human tissues • 1 human subject			• 1.7 x Higher SNR in 7 T vs 3T • T2* in 7T is half that in 3T	7T/3T	3D-UTE	GE	14min	20ms	64μsec	
Larson (2016)	• phantoms • 7 human subjects			• Similar SNR and CNR (~27) between UTE and ZTE	7T	3D-UTE/3D-ZTE	GE	UTE: 3min30s-4min/ ZTE: 4min30s-5min	UTE:1.4–1.9ms/ ZTE:1.1–1.7ms	UTE:76–80μs/ ZTE:16–20μs	192/320
Carl (2016)	• 1 human subject			• Increase in n. or spokes decrease scan time with lower SNR	3T	3D-Cones-IR-UTE	GE	15min-1.67min	50–80ms	0.03ms	256x256
Nazaran (2017)	• 4 human subjects	35	0	• Cortical bone can be seen with high contrast • T2* = 0.33–0.45ms	3T	3D-IR-UTE-Cones	GE	4.5min	116.7ms	0.032, 0.2, 0.4, 0.8 ms	128x128
Ma (2020)	• 6 human subjects • 2 human tissues			• UTE MRI shows trabecular bone with high contrast • T2* = 0.3–0.45ms	3T	3D-IR-UTE	GE	4min20s/ 10min	82ms	0.032ms-4.4	160x160
Biswas (2012)	• 8 animal tissues			• UTE bi-component analysis of cortical bone is feasible and suficient to describe bone compartments • UTE Short	3T	2D/3D-UTE	GE	14/250min	100/300ms	8μs/32μs	256x256

Study	Participants	Age	Female	Main Results	Field Strenght	MRI Sequence	Vendor	Scan Time	TR	TE	Matrix
				T2* = 0.29ms • UTE Long T2* = 2.81ms							
Bae (2012)	• 14 human tissues	58	7	• µ-CT porosity positively correlated with UTE total water (R2 = 0.23), free water (R^2 = 0.31), long T2* (R^2 = 0.25), short T2* (R^2 = 0.24)	3T	2D-UTE/3D-UTE	Siemens	27/250min	200/300ms	8µs	256x256
Horch (2012)	• 14 human tissues	70	6	High correlation between bound and pore water and mechanical properties							
Li (2014)	• 72 human subjects	54	42	• UTE Bone water positively correlated with age (R = 0.52) and negatively correlated (R = −0.57) with µCT bone mineral density. • UTE Suppression ratio positively correlated with µCT porosity (R = 0.88) and age (R = 0.87)	3T	Unsuppressed UTE, dual band suppressed UTE, IR-UTE	Siemens	15min			512x512
Marnhard (2015)	• 5 human subjects	26	3	• UTE quantitative maps of bound and pore water were created	3T	3D-UTE	Philips		2.5ms	0.065ms	
Rajapakse (2015)	• 16 human tissue • 34 human subjects	67	43	• UTE Porosity index correlated with µ-CT porosity (R^2 = 0.79), µ-CT pore size (R^2 = 0.81),µ-CT bone density (R^2 = 0.49; negatively), age (R^2 = 0.64), UTE pore water fraction (R^2 = 0.62), UTE bi-exponential T2* (R^2 = 0.64)	3T	3D-UTE	Siemens	115min	12ms	0.05–7.7ms	320x320
Chang (2015)	• 38 human tissues	65.7		• UTE Off-resonance saturation ratios correlated positively with µCT porosity and biomechanical properties • UTE short T2* = 0.35ms • UTE long T2*	3T	2D-UTE-MT	GE	12min	100ms	0.01–20ms	128x128

Study	Participants	Age	Female	Main Results	Field Strenght	MRI Sequence	Vendor	Scan Time	TR	TE	Matrix
				= 4.33ms • UTE T1 = 246ms							
Chen (2016)	• 6 animal tissues • 6 human subjects			• Bound water measured with 3D IR-UTE T2*~0.29 similar to T2* measured with 2D UTE and 3D-UTE	3T	• 3D IR-UTE • 2D-UTE • 3D-UTE	GE	2min		0.03–11ms	128x128
Abbasi-Rad (2017)	• 72 human subjects	55	42	• UTE $T1_{BW}$ = 162.47ms • UTE $T1_{FW}$ = 306.79ms • UTE BW_{conc} = 19.6% • UTE FW_{conc}= 5.6% • UTE $T1_{FW}$ and FW_{conc} positively correlated with age (R^2 = 0.72 and 0.62)	3T	3D-UTE dual echo subtraction	Siemens	6.6min	20/60ms	10/60ms	256 (read
Jerban (2017)	• 14 human tissues	47	4	• UTE MMF and T2* decreased 12% after cortical bone loading	3T	3D-UTE-Cones/3D-UTE-MT-Cones	GE		30ms	0.032–15ms	192x192
Jerban (2018)	• 18 human tissues	58	8	• UTE MMF correlated with μ-CT porosity (R = −0.67 to −0.73), μ-CT bone mineral density (R = 0.46 to 0.7)	3T	3D-UTE-MT-Cones	GE	15min	24.3ms	0.03–15ms	160x160
Jerban (2019)	• 156 human tissues	62	62	• UTE MMF correlated with μ-CT porosity (R = −0.72), μ-CT bone mineral density (R = 0.71), Young Modulus, stress (R = 0.6–0.61)	3T	3D-UTE-Cones/3D-UTE-MT-Cones	GE	30–40min	20ms	0.032	160x160
Jerban (2019)	• 11 human tissues	51	5	• UTE MMF and bi-component T2* can estimate variation in bone porosity bellow the image resolution range detectable by μ-CT	3T	3D-UTE-MT-Cones	GE	15min	24.3ms	0.03–15ms	160x160
Jerban (2019)	• 8 human tissues	63		• UTE Macromolecular proton density correlated with μ-CT porosity (R = −0.79), μ-CT bone mineral density	3T	3D-UTE-MT-Cones	GE	7min	24.3ms	0.03–15ms	160x160

Study	Participants	Age	Female	Main Results	Field Strenght	MRI Sequence	Vendor	Scan Time	TR	TE	Matrix
				(R = −0.7), age (R = −0.91)							
Hong (2019)	• 18 human tissues	67.5	12	• UTE Porosity index correlated with biomechanical stiffness (R = −0.79), infrared spectral imaging collagen conc. (R = −0.73), UTE BW (R = −0.95)	3T	3D-UTE	Siemens		12ms	0.05/2ms	320x320
Guo (2020)	• 12 human tissues			• UTE T1 bound water ~ 112.3ms in vivo	3T	3D IR-UTE	GE	60min	150–500ms	0.032ms/ 2.5ms	128x128
Jerban (2020)	• 35 human subjects	61		• UTE BWconc. measured by tricomponent T2* correlated significantly with μ-CT porosity (R = 0.7), biomechanical properties (R = 0.58–0.62)	3T	3D-UTE-Cones	GE	35min	28ms	0.032–24ms	160x160
Jerban (2020)	• 135 human tissues from 37 donors	61	19	• UTE TWconc. positively correlated with μ-CT porosity (R = 0.66), μ-CT pore size (R = 0.57), μ-CT bone marrow density (R = 0.71)	3T	3D-UTE-MT-Cones	GE	7min	24.3ms	0.03–15ms	160x160
Geiger (2014)	• 9 human subjects	85	3	• Average deviation of suface coordinates UTE vs μCT (0.19 ± 0.15mm) • Inter-rater ICC (UTE vs UTE) > 0.99	3T	3D-UTE	GE	60min	50ms	0.05ms	384x384
Ma (2018)	• 11 human tissues • 3 human subjects	86/38	7	• Glenoid diameters on CT, UTE not significantly different • Inter-rater ICC near perfect	3T	3D-IR-UTE-Cones	GE	15min	134ms	0.03ms	192x192
Finkenstaedt (2019)	• 4 human cadavers • 2 human subjects	54	3	• GRE sensitivity = 0.75, specificity = 1 • UTE sensitivity and specificity = 1 • UTE diagnostic confidence > GRE	3T	3D-UTE-Cones	GE	3min12s	44.3ms	0.05ms	256x256

Study	Participants	Age	Female	Main Results	Field Strenght	MRI Sequence	Vendor	Scan Time	TR	TE	Matrix
Huber (2020)	• 19 human subjects	75.3	11	• Intermodality kappa = 0.81 • Inter-rater agreement = 0.81	3T	3D-UTE PETRA	Siemens	5min15s	5ms	0.07ms	
Afsahi (2021)	• 12 human subjects	38	3	• Bland-Altman Limits of agreement: all differences (UTE vs CT) included within 95% CI	3T	3D-Slab-Selective-UTE	GE	~9min	2ms	0.028ms	
Schwaiger (2021)	• 30 human subjects	65	12	Sensitivity, specificity, accuracy: • 0.95, 0.98, 0.97 for GRE vs CT • 0.91, 0.96, 0.95 for UTE vs CT • Agreement and image quality was higher for GRE than UTE • Inter-rater agreement substantial to excellent	3T	3DT1SGRE/3D-UTE	Philips	GRE:5.12min / UTE: 6.3min	GRE:7.8ms/ UTE:6.3ms	GRE:2.3ms/ UTE:0.14ms	
Deininger-Czermak (2021)	• 27 human cadavers	73	11	• High Morphological Correlation MRI vs CT • UTE and GRE underestimated degeneration • SNR higher on UTE and GRE vs CT	3T	2D-UTE dual echo subtraction/3D FRACTURE (GRE)	Philips	UTE:8min56s/ GRE: 6min48s	UTE:10.2ms/ GRE:20.7ms	UTE: 0.2,4.6ms/ GRE:4.61ms	
Ngyuen (2022)	• 12 human subjects	12.6	2	• Inter-reader agreement kappa = 0.91–0.93 • Sensitivity and specificity were equivalent between TSE MRI and UTE (0.95–1) • UTE improved agreement on fracture detection but reduced agreement on management	3T	3D-UTE (PETRA)	Siemens	7min	6.5ms	0.07ms	256x128/
Breighner (2017)	• 34 human subjects	40	8	• Inter-rater and intermodality agreement (ZTE vs CT) kappa or ICC > 0.6	3T/1.5T	3D-ZTE	GE	4–6min	1.3/1.6ms	0	256 or 32
Argentieri (2018)	• 34 human subjects	57	17	• Inter-rater kappa = 0.72 • High intermodality agreement ZTE vs CT (86%	3T	3D-ZTE	GE	5min	417ms	0	320x320

Study	Participants	Age	Female	Main Results	Field Strenght	MRI Sequence	Vendor	Scan Time	TR	TE	Matrix
				within 1 grade of stenosis between ZTE and CT)							
Breighner (2019)	• 23 human subjects	28	18	• Interrater ICC = 0.6–0.99 • Intermodality ZTE vs CT ICC: 0.61–0.9	3T	3D-ZTE	GE	5min	425–528ms	0	512x512
Yuan (2019)	• 39 human subjects	11	19	• ADC were smilar on EPI and RUFIS with improved imaging quality without noise	3T	RUFIS	GE	3–6min	2.3ms	0	128x128x
de Mello (2020)	• 6 human tissues • 10 human subjects	39	2	• Interrater ICC = 0.92–0.98 • Intermodality ICC ZTE vs CT = 0.94–0.99 • Bland-Altman differences ZTE vs CT = 0.3–0.8mm	3T	3D-ZTE	GE	3–13min	0.8–1.1ms	0	512x512
Sandberg (2020)	• 95 human subjects	12	42	• High intermodality agreement (Z = −1.8) • Inter-rater agreemenet kappa = 1	3T	3D-ZTE	GE	86–171s	303–628ms	16μs	200x200/
Lee (2020)	• 20 human subjects	37	13	• High intermodality and interrater agreement (kappa: 0.8–0.9)	3T	3D-ZTE	GE	5min	785ms	0	260x260
Jeong (2020)	• 22 human subjects	60	9	• Sensitivity of ZTE: 0.9 and 0.93 • Moderate to strong correlation Hounsfield vs MR signal (R = 0.42 to 0.72)	3T	3D-PETRA	Siemens	3min29s	3.3ms	0.07ms	320x320
Sandberg (2020)	• 39 human subjects	11	19	• ADC were smillar on EPI and RUFIS	3T	RUFIS	GE	3–6min	2.3ms	0	128x128x
Ma (2021)	• 1 human subject	55	0		3T	3D-ZTE	GE	9min58s	1200ms	0	256x256x
Amar (2021)	• 7 human subjects	50	2	• High intermodality agreement ZTE vs CT (0.66 to 1.0)	3T	3D-ZTE/ Conventional MRI sequences	GE				
Bharadwaj (2021)	• 100 human subjects	40	44	• ZTE had higher image quality, diagnostic confidence than SPGR	3T	3D-ZTE	GE		0.5ms	0	256x128
Li (2022)	• 40 human subjects	40	17	• ZTE accuracy, interreader and intermodality agreement were	3T	3D-ZTE/ T1FSE	GE	2–3min	553–777ms	6.8–7.2ms	320x320

Study	Participants	Age	Female	Main Results	Field Strenght	MRI Sequence	Vendor	Scan Time	TR	TE	Matrix
				higher than T1FSE							
Hou (2022)	• 22 human subjects	52	14	• ZTE performance and interreater agreement was higher	3T	3D-ZTE/ Conventional MRI sequences	GE	ZTE: 5min	ZTE: 1020ms	0	300x370
Gyftopoulos (2013)	• 3 human tissues	52	3	• No significant differences between T1FLASH and CT	3T	T1FLASH	Siemens	3min28s	10ms	2.45/3.7ms	192x192
Gyftopoulos (2014)	• 15 human subjects	28	2	• No significant differences between T1FLASH and arthroscopy	3T	T1FLASH	Siemens	3min28s	10ms	2.45/3.7ms	192x192
Ang (2017)	• 24 human subjects	19	2	• Sensitivity, specificity and accuracy of T1VIBE = 97.7, 92.3, and 95.7 %, respectively	3T	T1VIBE	Siemens		7ms	2.45ms	
Stillwater (2017)	• 11 human subjects	29	3	• Measurements of T1VIBE and CT were equivalent	3T	T1VIBE	Siemens	4min16s	10.5ms	3.5ms	256x100
Koh (2017)					1.5T/3T	T1VIBE	Siemens		6–8ms	3–5ms	
Samin (2019)	• 17 human subjects	37	8	• High intermodality agreement T1FLASH vs CT (89.5%)	3T	T1FLASH	Siemens		10ms	2.4ms	192x100
Gersing (2019)	• 32 human subjects	33.9	17	• Intermodality agreement GRE and Radiograph (periosteal reaction: 0.67, destruction: 0.75), sensitivity (86.2%)	3T	T1wGRE	Philips	5min30s to 6min45s	10ms	2.7ms	
Subramanian (2021)	• 50 human subjects	27	37	• No significant differences in measurements T1VIBE and CT	3T	T1VIBE	Siemens	3min	6.9ms	2.6ms	480x150
Johnson (2021)	• 6 human subjects	14	0	• High quality CT-like contrast MRI	3T	FRACTURE	Philips	4min56s	50ms	2.3–13.8ms	
Boker (2017)	• 54 human subjects	56	26	• Sensitivity, specificity of SWI (1.0/0.95) vs conventional MRI sensitivity (0.2)	1.5T	SWI-MRI	Siemens	5min11s	49ms	14ms	
Norenberg (2017)	• 44 human subjects	52	18	• Detection rates, sensitivity, specificity SWI: 0.91, 0.977, 0.913 vs Standard MRI:	1.5T	SWI-MRI	Siemens	4min30s	49ms	20ms	256x256

Study	Participants	Age	Female	Main Results	Field Strenght	MRI Sequence	Vendor	Scan Time	TR	TE	Matrix
				0.478, 0.48, 0.81							
Bender (2017)	• 81 human subjects	50	40	• SWI: sensitivity, specificity, correlation (0.989, 0.991, 0.96, 0.95)	1.5T	SWI-MRI	Siemens	5min11s	49ms	14ms	448x448
Boker (2018)	• 39 human subjects	67	24	• Sensitivity, specificity of SWI higher than conventional MRI in all morphologic features	1.5T	SWI-MRI	Siemens	5min11s	49ms	20ms	
Ulas (2019)	• 37 human subjects	60.1	27	Accuracy: • SWI(0.912) • T1w +SWI (0.938) • T1w alone (0.888)	1.5T	SWI-MRI	Siemens	5min3s	49ms	20ms	192x192
Engel (2019)	• 21 human subjects	51.8	12	• Sensitivity, specificity of SWI (0.966/0.995) vs conventional MRI (0.431/1.0)	1.5T	SWI-MRI	Siemens	5min11s	49ms	14ms	
Boker (2019)	• 53 human subjects	54.5	26	• Sensitivity, specificity of SWI (1.0/0.96) vs conventional MRI (0.79/0.83) for osteoblastic lesions	1.5T	SWI-MRI	Siemens	5min2s	49ms	20ms	
Boker (2020)	• 40 human subjects	47.1	17	• Higher accuracy to measure hip angles than radiographs	1.5T	SWI-MRI	Siemens	4min37s	49ms	20ms	
Deppe (2021)	• 68 human subjects	40.5	28	• Sensitivity SWI (0.82) was higher than T1 (0.73) • Agreement with CT for SWI (0.92) vs T1 (0.84)	1.5T	SWI-MRI	Siemens	5min47s	49ms	14ms	448x244
Ulas (2022)	• 36 human subjects	54	24	• SWI specificity (0.9) was higher than T1 (0.4) and VIBE/T1 (0.5) • VIBE overestimated lesions	1.5T	SWI-MRI	Siemens	5min3s	34ms	15ms	384x252
Morbée (2021)	• 30 human subjects	40	16	High intermodality, inter-rater, and intra-rater agreement with CT	3T	3D T1 Multi-echo GRE FLASH with CAIPIRINHA	Siemens	4min3s	7ms	2/3.5ms	288x288
Staartjes (2021)	• 11 human subjects			High intermodality	3T	3D T1 Multi-echo GRE FLASH	Siemens	3min53s	7ms	2.1/4.1ms	288x288

Study	Participants	Age	Female	Main Results	Field Strenght	MRI Sequence	Vendor	Scan Time	TR	TE	Matrix
				agreement with CT							
Forkflow (2021)	• 30 human subjects		0	High intermodality, inter-rater, and intra-rater agreement with CT	3T	3D T1 Multi-echo GRE FLASH	Philips	2min38s	6.5ms	2.1–4.8ms	448x448x
Willemsen (2021)	• 8 human tissues	78	4	Higher intermodality and inter-rater agreement sCT vs micro-CT	3T		Philips	2min31s	6.9ms	2.1–4.4ms	
Jans (2021)	• 40 human subjects		14	sCT diagnostic accuracy higher than T1wMRI (0.94, 0.97, 0.92 vs 0.86, 0.81, 0.84)	3T	3D T1 Multi-echo GRE FLASH	Siemens	5min37s	7ms	2/3.5ms	384x384
Lena (2022)	• 9 human subjects		3	High intermodality agreement with CT	1.5T	3D T1 Multi-echo GRE FLASH	Philips	3min	7ms	2.1/4.2ms	

Table 2.

Suggested Protocols for synthetic CT imaging using UTE, ZTE, GRE MRI, and Deep Learning.

	Field Strenght	MRI Sequence	TR (ms)	TE (ms)	Matrix	Slice Thickness (mm)	BW (KHz)	Additional Parameter
UTE	3T	• 3D-UTE • 3D-IR-UTE*	80–100	0.03–0.05	192x192	3	62.5	*IR time: 20 – 50 ms
ZTE	3T	3D-ZTE	1–1.4	0	320x320	1	62.5	
GRE FLASH	3T	Dixon-T1-FLASH	10	2.45/3.7	192x192	1	76.8	
GRE VIBE	3T	T1-VIBE	10.5	3.5	256x100	0.7	76.8	
SWI	3T	SWI-MRI	49	14	448x448	3		
Deep Learning	3T	3D-Multi-echo GRE FLASH	7	2.1/4.1	288x288	0.6–1	144	Network architecture: U-net or GAN

TR: Time of recovery; TE: Time echo; BW: Bandwidth; IR: Inversion recovery; GRE: Gradient echo; FLASH: Fast low angle shot; VIBE: Volumetric interpolated breath-hold; SWI: Susceptibility weighted imaging; GAN: Generative adversarial networks